Spectrochimica Acta Part B 60 (2005) 1280 – 1307

SPECTROCHIMICA ACTA PART B

www.elsevier.com/locate/sab

Effect of laser parameters on laser ablation and laser-induced plasma formation: A numerical modeling investigation

Annemie Bogaerts *, Zhaoyang Chen

University of Antwerp, Department of Chemistry, Universiteitsplein 1, B-2610 Antwerp, Belgium

Received 12 April 2005; accepted 20 June 2005
Available online 26 July 2005

Abstract

A comprehensive numerical model has recently been developed for nanosecond (ns) laser ablation of metallic targets, describing the processes of target heating, melting and vaporization, the resulting plume expansion in 1 atm helium gas, as well as plasma formation in the plume. In the present paper, we investigate the influence of laser parameters, i.e., laser irradiance, pulse duration and wavelength, on typical calculation results, such as the target temperature, melt and evaporation characteristics, the plume expansion velocity, plume (plasma) temperature and ionization degree, densities of neutrals, ions and electrons in the plume, as well as the laser absorption characteristics in the plume (plasma shielding). Comparison is made with experimental data from literature, whenever available, and in general, good agreement is reached between our model predictions and experimental results. Therefore, the model can be useful to predict trends in target and plume (plasma) characteristics, which are difficult to obtain experimentally.

Keywords: Laser ablation; Laser-induced plasma; LIBS; Modeling; Plume expansion; Laser parameters; Laser absorption

1. Introduction

Lasers are widely applied in analytical spectrometry, for the analysis of solid materials. Several analytical techniques make use of the effects of laser–solid interaction, in different regimes of laser irradiance, including matrix assisted laser desorption ionization (MALDI) (e.g., [1]), laser microprobe mass spectrometry (e.g., [2]), laser-induced breakdown spectrometry (LIBS) (e.g., [3–5]), as well as laser ablation (LA) used as sample introduction method for inductively coupled plasma mass spectrometry (LA–ICP-MS) or atomic emission spectrometry (LA–ICP-AES) (e.g, [6–8]).

LIBS and LA for sample introduction in the ICP make use of similar laser operating conditions. Typically, Nd:YAG lasers (with wavelengths ranging from 1064 nm down to the UV range) or excimer lasers (in the UV range) are applied. Typical pulse durations are in the order of several nanoseconds (ns), although there is a trend to scale down to fs-pulse duration, and the laser irradiance varies from 10^8 till above 10^{10} W/cm^2. Generally, the evaporated plume expansion takes place in 1 atm background gas, for instance in He, Ar or air.

Consequently, although LIBS and LA are based on different mechanisms of detection, the processes occurring during and after laser–solid interaction are quite similar. In the case of metallic targets, the laser causes heating of the solid target, followed by melting and evaporation of some of the target material. The evaporated material expands, and because of the high temperature, a plasma is formed in the material plume. This plasma contains electrons, ions, neutral species, as well as excited species. The emission of light originating from the excited species in the plasma constitutes the analytical signal measured by LIBS. During the plume expansion, the temperature drops down, and eventually, the evaporated atoms will undergo condensation, resulting in the formation of nm-sized particles. Besides, also larger (μm-sized) particles can be formed, e.g., by

* Corresponding author. Fax: +32 38202376.
E-mail address: annemie.bogaerts@ua.ac.be (A. Bogaerts).

0584-8547/$ - see front matter © 2005 Elsevier B.V. All rights reserved.
doi:10.1016/j.sab.2005.06.009

splashing of the molten target, due to the recoil pressure of the material plume. In the case of LA as sample introduction method for the ICP, these particulates are transported, in the form of aerosols, from the laser plume into the ICP, where they will be vaporized (atomized) again, as well as ionized and/or excited, and subsequently measured with mass spectrometry or atomic emission spectrometry.

Recently, we have developed a comprehensive numerical model, which describes the processes occurring during the laser ablation of metallic targets, and the subsequent expansion of the evaporated material plume, as well as plasma formation. The original model was developed for expansion in vacuum [9,10], and was subsequently extended for expansion in 1 atm He gas, which appeared to be a much more complicated task [11,12]. The model does not yet include mechanisms for particle formation, but this task is planned for the next stage.

It is worth to mention that there exist a variety of models in literature for laser ablation under vacuum (or low pressure, i.e., up to 100 Pa) conditions (for a comprehensive literature overview, see Ref. [10]). However, the number of models that have been developed for laser ablation under 1 atm background gas pressure, is very limited, and these model investigations [13–17] often apply the hydrodynamic equations only for the vapor species, like in vacuum conditions, whereas it is obvious that a binary gas mixture (i.e., metal vapor and background gas), as well as the interactions between vapor and gas, need to be considered. A hydrodynamic model, which describes the behavior of both vapor and background gas, has been developed by Gnedovets and Gusarov, and it is applied to expansion in a background gas at 1 atm, but for a long laser pulse (ms-range) at very low laser irradiance (i.e., 10^4–10^5 W/cm^2), so that no plasma is formed [18–20]. Recently, Gusarov and Smurov have applied this model to shorter laser pulses (ns-range) at a laser irradiance in the order of 10^9 W/cm^2, hence conditions typical for LA and LIBS, but without taking into account the formation of a plasma [21]. It is, however, clear that plasma formation is important at these conditions. To our knowledge, there exist no models yet that describe the laser ablation with expansion in 1 atm background gas, including the plasma formation, except for the model developed in our group [11,12].

In the present paper, we have applied our model to a wide range of laser operating conditions, i.e., laser irradiance, pulse duration and wavelength, which are typical for LIBS and LA as sample introduction method for the ICP.

There are many experimental studies reported in the literature, about the effect of laser parameters on the evaporation process, plume and plasma characteristics, and analytical performance of LIBS, LA–ICP-MS and LA–ICP-AES. Russo and co-workers [22–24] have investigated the effect of laser irradiance on electron density and plume temperature, for a Nd:YAG laser at 266 nm and glass or Si samples, in the irradiance range of 10^9–8×10^{10} W/cm^2, and they have derived a simple scaling law, with a different behavior below or above 2×10^{10} W/cm^2. In Ref. [25], the effect of laser irradiance, in the range of 1.2–3×10^8 W/cm^2, on the electron density is reported, but for plume expansion in vacuum. Russo's group has also studied the effect of laser irradiance on the mass ablation rate of Cu [26], and they found a different power law, for a laser irradiance below or above 3×10^8 W/cm^2, attributed to plasma shielding. Moreover, still a different irradiance behavior was observed at a laser irradiance above 10^{10} W/cm^2, probably due to self-focusing or phase explosion [24,27]. Another scaling law, for the relation between mass ablation rate on one hand, and laser irradiance and wavelength on the other hand, was presented in Ref. [28]. The effect of laser fluence on the ablation rate was also reported by Horn et al. [29], up to a fluence of about 45 J/cm^2, for a Nd:YAG laser at 266 nm and an excimer laser at 193 nm, in He or Ar background gas, and a range of different sample materials, and it was found that the ablation rate increases linearly with fluence [29]. The influence of laser irradiance on the temporal evolution of the plasma is studied by Laserna et al. with a dynamic microphone, for a Nd:YAG laser at 1064 nm, in the irradiance range of 10^9–10^{10} W/cm^2, and it is observed that a higher laser irradiance yields larger plasma volumes [30]. Shannon et al. and Chan and Russo [26,31] have described the effect of laser irradiance on the ICP emission intensity, with an excimer laser at 248 nm and a Nd:YAG laser at 266 nm, for several different sample types, and laser irradiance values ranging from 10^7 W/cm^2 till above 10^{10} W/cm^2. It is found that the signal intensity as a function of laser irradiance exhibits two different slopes, with a steeper slope below a certain irradiance value, and a smaller slope above this value [26,31]. The value of this irradiance depends on the laser pulse duration, i.e., it is higher for ps than for ns pulses. This roll-off behavior is again attributed to plasma shielding (see above) [26,31]. The same authors have also reported the effect of laser irradiance on the measured particle size distributions [32] and on elemental fractionation [33]. The fraction of larger particles seems to decrease as a function of laser irradiance, up to a value of 4–5×10^8 W/cm^2, which is found to be similar to the threshold value for plasma shielding [32]. Above this value, the particle size distribution remains more or less unchanged, but the total number of particles keeps increasing [32]. Furthermore, it is observed that fractionation occurs for a laser irradiance below 6×10^8 W/cm^2, and above 2×10^{10} W/cm^2, but it is found to be unimportant in the region in between [33]. In Ref. [34] it is shown that the lifetime of clusters in the plasma is reduced at higher laser irradiance. Finally, Sdorra and Niemax have studied the effect of laser energy, in the range of 2–20 mJ/pulse, for a Nd:YAG laser of 1064 nm and five different background gases, and it was reported that the measured plasma temperature and the emission intensity in the laser induced plasma generally increase with laser energy [35].

The effect of laser pulse duration on laser induced plasma emission, electron density and plume temperature is reported in Refs. [36–38]. In Ref. [36], an excimer laser at 248 nm is used, and comparison is made between a pulse duration of 50 ps and 10 ns full-width at half-maximum (fwhm), at fixed laser fluence, hence different laser irradiance. Calculations with a plasma ablation model show that in the initial plasma, both temperature and electron density are found to be significantly higher for the 50 ps pulse, because of the higher laser irradiance. However, at later times, not much difference is observed between the pulses of 50 ps and 10 ns, and it seems that the plasma characteristics then depend on the total energy deposited, and not on the pulse duration [36]. In Ref. [37] comparison is made between a pulse of 10 ns and 35 ps, with a Nd:YAG laser at 532 and 1064 nm, for high laser irradiance, and it is found that the plume temperature and electron density, as well as the plume expansion velocity, increase drastically for the ps-pulse, compared to the ns-pulse [37]. In Ref. [38], laser pulses of 500 fs, 5 ps and 270 ps fwhm, of a Ti:sapphire laser are compared, at very high laser irradiance. The measured excitation temperature was found to be higher for the longer pulses, but the electron density was observed to be independent from the laser pulse duration, at constant fluence, at a delay time of several μs [38]. The effect of laser pulse duration on the ablation rate is described by Mao et al. [39,40], for an excimer laser at 248 nm with 30 ns pulse duration, and a Nd:YAG laser at 1064, 532 and 266 nm, with 3 ns or 35 ps pulse duration, at constant laser energy (in the order of 5 mJ). Shorter pulses appear to give rise to more efficient laser ablation [39]. The mass ablation rate for the 35 ps pulse is an order of magnitude higher than for the 30 ns pulse, which is attributed to different mechanisms, i.e., thermal vaporization in the ns-pulse range vs. non-thermal mechanisms for ps-laser pulses [40]. Hence, in the ns-regime, there seems to be more energy lost in the sample by thermal dissipation, and less energy is converted to ablated mass. Moreover, plasma shielding is expected to be more predominant in the ns-range [39].

In the same papers [39,40], also the influence of laser wavelength is discussed. It is found that the mass ablation rate at the wavelength of 266 nm is an order of magnitude higher than at 1064 nm [40]. Also the ICP emission intensity seems to be significantly higher at 266 nm than at 532 and 1064 nm [39]. This is attributed to stronger plasma shielding and a higher target reflectivity at IR wavelengths, leaving less laser energy available for target evaporation [39]. The same authors also reported a lower fluence threshold for mass ablation, and a more controlled ablation rate, at shorter wavelengths [41]. Laserna and coworkers, on the other hand, observed a lower fluence threshold at 1064 nm and 532 nm, compared to 266 nm, for different metals, because the laser induced breakdown is favored at longer wavelengths, due to inverse Bremsstrahlung being more efficient with IR wavelengths [42]. Horn et al. [29] observed no clear dependence of the measured ablation rate on laser wavelength, but the comparison was made between an excimer laser at 193 nm and a Nd:YAG laser at 266 nm, hence different laser types, so that other effects might also play a role, and moreover, the laser wavelengths are lying relatively close to each other. According to the empirical formula derived in Ref. [28], based on experiments for laser wavelengths at 1064, 532 and 266 nm, the mass ablation rate varies with $\lambda^{-4/3}$, hence longer wavelengths correspond to a reduced mass ablation. Günther et al. studied the effect of wavelength on the particle size distribution, by making use of a Nd:YAG laser at 266, 213 and 193 nm, and an excimer laser of 193 nm [43,44]. They observed that shorter wavelengths give rise to smaller particles, which they attribute to a lower penetration depth inside the target (i.e., silicate glasses) for the shorter wavelengths. Because of the larger fraction in small particles, more particles will be completely vaporized in the ICP, resulting in less fractionation at shorter wavelengths [43,44]. The effect of laser wavelength on elemental fractionation was also investigated by Gonzales et al., with a Nd:YAG laser of 266 and 213 nm, and an excimer laser of 193 nm [45], and it was found that the fractionation is strongly dependent on laser and sample parameters.

The influence of laser wavelength on the electron density and plume temperature was also reported in a few papers. In Ref. [46], a Nd:YAG laser of 1064, 532 and 355 nm was applied, and the electron density and temperature were measured as a function of position from the target. The laser irradiance needed for plasma formation appeared to be much higher for the 1064 nm wavelength than for the 532 and the 355 nm wavelength [46]. Finally, Detalle et al. have compared a Nd:YAG laser at 1064 nm and 6 ns pulse duration, with an Er:YAG laser at 2940 nm and a pulse of 170 ns fwhm, at a laser irradiance of 4×10^{8} W/cm^2, and they investigated the effect of He or air as background gases on the measured plasma temperature and electron density [47]. With the Nd:YAG laser, the plasma temperature was found to be very similar for expansion in He and air, but with the Er:YAG laser, the temperature was somewhat higher for He than for air. The measured electron density was observed to be higher for air than for He, and moreover, in He similar results were obtained for both lasers, whereas in air, some differences were observed between the Nd:YAG and Er:YAG laser [47].

It is the goal of our present paper to investigate in detail and systematically the effect of laser irradiance, pulse duration and wavelength, on the target, plume and plasma behavior, during and after laser–solid interaction, in order to obtain a better insight in the exact influence of these laser parameters. We hope to be able to verify and quantify the explanations and suggestions made from experimental observations, and ultimately to assist the experimental research going on in different laboratories, in finding optimum laser conditions for good analytical practice.

2. Description of the model

The model for laser ablation of a Cu target in 1 atm He gas was explained in detail in Ref. [12]. Hence, in the present paper we will not formulate the equations again, but we will only briefly summarize qualitatively the various processes which are described in the model.

The heating of the Cu target, as a result of laser–solid interaction, is described with a heat conduction equation, which yields the temperature distribution inside the target, as a function of time. When the temperature rises above 1358 K (i.e., melting point of Cu), the Cu target starts melting, and the same heat conduction equation is used for the molten phase, but using the appropriate thermal data for liquid Cu. When the temperature rises further, vaporization can become significant, and the vaporization pressure is calculated from the surface temperature, by integrating Clausius–Clapeyron equation. The vapor pressure yields the vapor density at the surface, and this is used as input (i.e., boundary condition) in the second part of the model, together with the vapor velocity and temperature at the surface.

The expansion of the evaporated Cu material into 1 atm He background gas is described with Navier–Stokes equations, for conservation of total mass density, vapor mass density, momentum and energy, in a binary gas mixture. This set of equations is much more complicated than the corresponding set of equations for expansion in vacuum [10], because it contains gas mixing terms, i.e., thermal conductivity, viscosity and diffusion. Hence, it appeared to be much more difficult to solve these equations. A more detailed explanation, also with respect to the appropriate use of boundary conditions, is given in Ref. [12].

Because of the high temperature in the expanding plume, a plasma is created, resulting in the formation of electrons and ions of the Cu vapor and He gas. For the typical conditions of LA and LIBS, the temperature can be so high that beside Cu^+ ions also Cu^{2+} ions are formed. The first-order and second-order ionization of Cu (i.e., the ratio of Cu^+/Cu^0 and of Cu^{2+}/Cu^+, respectively) and the first-order ionization of He, are calculated with Saha–Eggert equations, because the plasma is considered to be in local thermal equilibrium. From the calculated fraction of Cu^+, Cu^{2+}, Cu^0, He^+, He^0 and electrons, in combination with the calculated densities of Cu vapor and He background gas, the densities of these species are computed.

Finally, because of the formation of a plasma in front of the target, the laser beam will be partially absorbed before it reaches the target, i.e., so-called “plasma shielding”. The three dominant absorption mechanisms are electron–ion and electron–neutral inverse Bremsstrahlung and photo-ionization of excited atoms. Inverse Bremsstrahlung involves the absorption of a photon by a free electron. The electron is raised to a higher state in the continuum. This process must occur within the field of a heavy particle (ion or neutral), so that momentum is conserved. The formulas for the absorption coefficients of these processes are presented in Ref. [10,12], and also later in this paper (Section 3.1.3). Based on these absorption coefficients, the laser irradiance reaching the target, i.e., after plasma shielding, is calculated.

The different parts of the model are strongly coupled, because the target evaporation determines the plume expansion, and the plume affects the target as well. Hence, the boundary condition for the target part has to be obtained from the plume part, and vice versa [12]. Moreover, the absorption of the laser beam in the plasma affects the laser–solid interaction, because the laser energy reaching the target can be considerably attenuated, and it also influences the plume temperature (i.e., gain and loss terms in the energy conservation equation). Therefore, the various parts of the model need to be solved simultaneously as a function of time, in order to obtain an overall picture of the laser–solid interaction, followed by plume expansion and plasma formation. More quantitative details about the complete model can be found in Ref. [12].

3. Calculation results and discussion

The calculations are performed for different laser wavelengths and pulse durations, and for a wide range of laser irradiance. The laser pulse is assumed to have a Gaussian time-profile, and always starts at 0 ns. Calculations are always carried out until 100 ns. The reason is that the model is one-dimensional, hence it assumes forward expansion of the vapor plume, which is only a reasonable assumption for the early stage, e.g., until an expansion distance of about 1 mm (depending on the laser beam spot size) [18,37,48,49]. At later stages, expansion in the radial direction will become important, so that our model will have to be extended to two dimensions (radial symmetry), in order to describe the expansion process. The target is assumed to be pure Cu, and the expansion takes place in 1 atm He gas. Table 1 given an overview of the laser ablation conditions to which the model is applied.

3.1. Effect of laser irradiance

The laser irradiance is varied from 10^8 till 10^{10} W/cm^2, because these are typical values used for LIBS and LA. Indeed, at lower values, no melting and certainly no vaporization is taking place. At higher values, on the other

Table 1
Overview of the laser ablation conditions to which the model is applied

Target	Copper
Background gas	Helium (1 atm)
Laser irradiance	10^8–10^{10} W/cm^2
Laser pulse duration	0.3–30 ns
Laser wavelength	266–532–1064 nm

hand, some additional processes will probably become important, for instance explosive boiling [50–52], which are not yet included in our model. The laser wavelength and pulse duration are kept fixed here at 266 nm and 5 ns fwhm.

3.1.1. Target heating, melting and vaporization

Fig. 1 shows the calculated temperature distributions inside the target, as a function of time during and after the laser pulse, for three different values of laser irradiance. In all cases, the temperature reaches a maximum at the surface, at about 10 ns, which means during the laser pulse, and it drops gradually deeper inside the target. However, at 100 ns, our calculations predict still some temperature elevation until a depth of about 10 μm in the target. At 10^8 W/cm^2 (Fig. 1a) the maximum surface temperature is about 1500 K. This temperature is too low to yield an appreciable amount of melting, because the melting point of Cu is 1358 K.

At 10^9 W/cm^2 (Fig. 1b) the calculated surface temperature reaches a maximum of about 8000 K. At this high temperature, melting takes place, and the upper 1.8 μm of the target surface becomes in liquid (molten) phase, as is visualized in the figure below the temperature distribution plot. After about 50 ns, the melt depth starts decreasing again, because of the temperature drop, but at 100 ns, the upper surface layer is still in molten phase.

At 10^{10} W/cm^2 (Fig. 1c) the surface temperature is calculated to reach a maximum of about 15,000 K. This is extremely high, and probably overestimated. Indeed, we expect that other target processes, such as explosive boiling, could then play a role, and will reduce the temperature by loss of excessive heat. It is, indeed, stated that explosive boiling starts at 2×10^{10} W/cm^2 for Si [50,51], and at 5×10^{10} W/cm^2 for Al [52]. This process is, however, not yet taken into account in our model, so we should keep in mind that the resulting temperature is most probably too high. The overestimated surface temperature may also be the result of an impropriate boundary condition for the plume velocity at the target. Indeed, as will be shown below, we calculate a negative plume velocity at the target during the laser pulse. This brings some extra energy from the plume into the target, which is maybe not realistic. In the near future, we plan to revise the boundary condition (which is a very complicated aspect of the model), and to include explosive boiling, in order to be able to calculate a more realistic surface temperature at very high laser irradiance.

At the high surface temperature, as calculated for the case of 10^{10} W/cm^2, the molten phase extends till about 3.3 μm inside the target, as is clear from the figure below the temperature distribution plot, and resolidification of the liquid phase does not yet take place at 100 ns, because the target surface temperature is still above 2000 K. Again, this melt depth may be somewhat overestimated, because of the too high surface temperature.

In Fig. 2, the calculated maximum surface temperature, maximum melt depth, maximum evaporation rate and evaporation depth are plotted as a function of laser irradiance. The corresponding laser fluence, for a laser pulse of 5 ns fwhm, is indicated at the bottom of the figure. For instance, a laser irradiance of 10^8, 10^9 and 10^{10} W/cm^2 corresponds here to a laser fluence of 0.532, 5.32 and 53.2 J/cm^2. The maximum surface temperature (Fig. 2a) and melt depth (Fig. 2b) increase more or less linearly with the logarithm of the laser irradiance, which means that the difference in temperature and in melt depth between 10^8 and 10^9 W/cm^2 is more or less the same as between 10^9 and 10^{10} W/cm^2. In other words, the effect of laser irradiance becomes smaller for higher values. The reason is the increased plasma shielding at higher laser irradiance, as will be shown later in

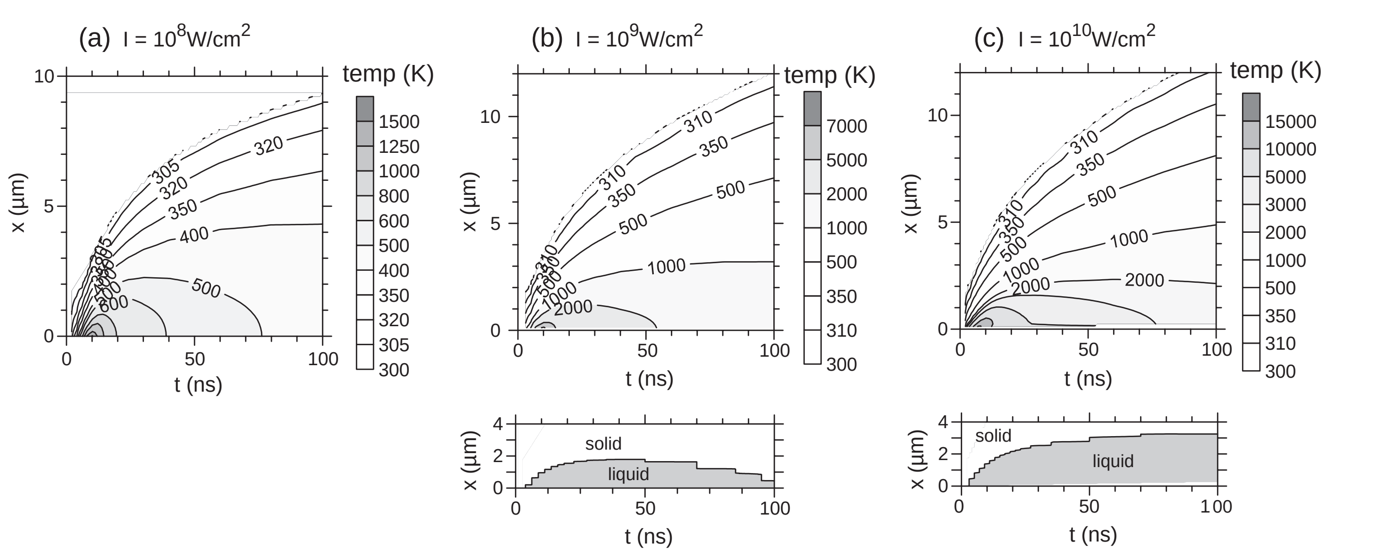

Fig. 1. Calculated temperature distributions inside a copper target, as a function of time during and after laser–solid interaction, up to 100 ns, for laser radiation of 266 nm and 5 ns (fwhm) pulse duration, at a laser irradiance of 10^8 (a), 10^9 (b) and 10^{10} W/cm^2 (c). Also shown are the regions of molten (liquid) phase, for this time-period, for the laser irradiance of 10^9 (b) and 10^{10} W/cm^2 (c). Note that at 10^8 W/cm^2 target melting was found to be negligible.

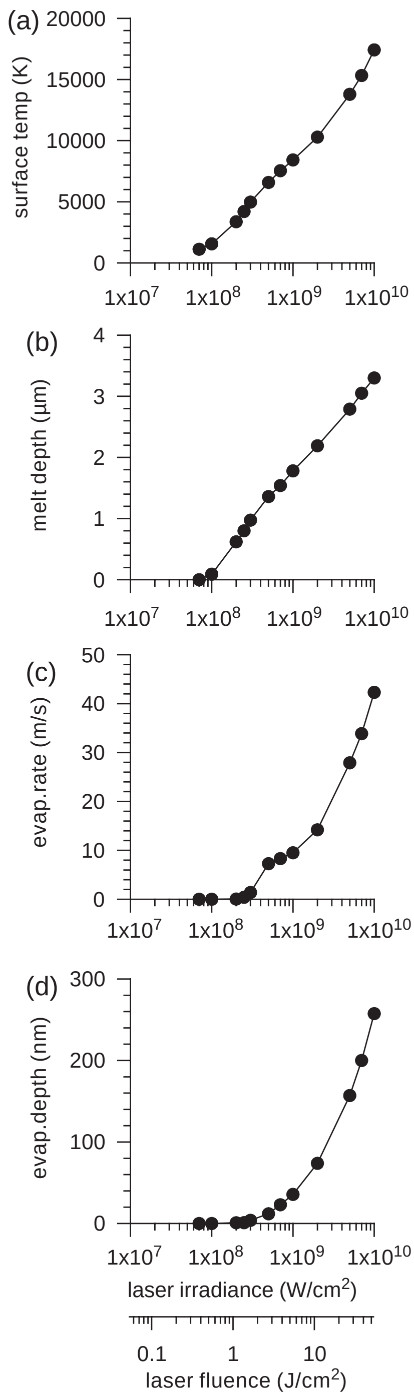

Fig. 2. Calculated maximum surface temperature (a), maximum melt depth (b), maximum evaporation rate (c), and total evaporation depth (d), as a function of laser irradiance, for laser radiation of 266 nm and 5 ns pulse duration. Also shown are the corresponding values of the laser fluence for this pulse duration (bottom of figure).

this paper, which reduces the effective laser energy reaching the target, and consequently the target heating. As was also illustrated in Fig. 1, melting occurs only for a laser irradiance above 10^8 W/cm^2, and the depth of molten phase is calculated to be in the order of a few µm, for the typical laser irradiance values applied in LIBS and LA.

The evaporation of target material becomes only appreciable for laser irradiance values above 3×10^8 W/cm^2, for the laser wavelength of 266 nm and pulse duration of 5 ns fwhm, as appears from the calculated evaporation rate (Fig. 2c) and evaporation depth (Fig. 2d) as a function of laser irradiance. The evaporation rate seems to increase rapidly until about 5×10^8 W/cm^2, and then more smoothly, as a function of laser irradiance, because plasma shielding starts to play a role above 5×10^8 W/cm^2 (see below). In general, the calculated evaporation rate and depth increase more or less linearly with laser irradiance (shown by the exponential rise on the logarithmic scale). For a laser irradiance of 10^9 W/cm^2, the maximum evaporation rate is calculated to be 9.5 m/s, corresponding to the total depth of 36 nm, after the laser pulse is finished. At 10^{10} W/cm^2, the calculated evaporation rate reaches a maximum of 42 m/s, yielding a depth of almost 260 nm.

Our calculated values for surface temperature, melt depth and evaporation depth are in good agreement with other modeling results reported in literature, albeit often for LA in vacuum. In Ref. [14] a model was applied for LA of Cu, Al and Au targets at 1 atm, for 26 ns laser pulses (laser wavelength not specified), in a fluence range between 1 and 25 J/cm^2, which corresponds to our fluence conditions (see Fig. 2). The maximum surface temperature, melt depth and ablation depth were calculated in the order of 3000–9000 K, 0–3 µm and 0–40 nm, respectively, increasing with fluence, which is in good correlation with our results. In Ref. [53] a surface temperature was calculated of about 5000 K, and the ablation depth per pulse was in the order of several nm, increasing with laser fluence (up to a value of 9 nm at 5 J/cm^2; hence somewhat lower than our results), for a 248 nm excimer laser with 26 ns fwhm. In Ref. [54] a model for a Nd:YAG laser of 355 nm with 6 ns fwhm and an Al target predicted a surface temperature slightly above 4000 K for a fluence of 9 J/cm^2, and the ablation depth ranged from 1 to 100 nm, for a fluence of 2–10 J/cm^2, hence in excellent agreement with our results. Finally, in Ref. [55] a melt depth was calculated in the order of 1–2 µm, for a Nb target and an excimer laser of 248 nm and 30 ns fwhm, at a laser irradiance of 5×10^8 W/cm^2, again in good correspondence with our results.

Experimentally, a number of papers have reported on measured crater depths for laser ablation. Niemax et al. have measured a crater depth in the order of 45 µm after 30 laser pulses, hence about 1.5 µm per pulse, for a laser pulse energy of 12 mJ, and a Cu sample at 1 atm He [35]. In Ref. [56] the measured crater depth of a Cu sample was about 0.65 and 1 µm per pulse for an excimer laser of 5 and 14 mJ, respectively. The laser fluence or irradiance was not specified in these papers, but from the crater diameter, we deduced a laser fluence of about 150 J/cm^2 in Ref. [35] and about 44 and 55 J/cm^2, respectively in Ref. [56]. These values are higher than the fluence range investigated in our paper, and from the significant rise of calculated evaporation depth with laser irradiance (or fluence) in Fig. 2, it can be concluded that our calculated values are in the correct order of magnitude. Moreover, Horn et al. [29] have reported on measured crater depths for Cu samples in the order of 10–20 μm after 100 pulses, hence about 100–200 nm per pulse, with a 266 nm Nd:YAG laser, at a fluence of 23 J/cm^2 or 3.8×10^9 W/cm^2, which is in excellent agreement with our calculated evaporation depth of Fig. 2. Hence, although liquid splashing of the molten material will occur as well, the good correlation between our calculated evaporation depths and the measured crater depths indicates that the target ablation seems to be mainly caused by evaporation, at least in the range of laser irradiance under investigation here, and that our model, in the present stage, can present a realistic picture of the laser ablation process.

3.1.2. Evaporated plume expansion and plasma formation

The calculated behavior of the expanding vapor plume is illustrated in Fig. 3, for three different values of laser irradiance, i.e., 3×10^8 W/cm^2 (which means just above the threshold for target vaporization, at the conditions under study, cf. Fig. 2), 10^9 and 10^{10} W/cm^2. At 10 ns, i.e., during the laser pulse, the Cu vapor density (Fig. 3a) a is at maximum at the target, and drops steeply as a function of distance from the target. At later times, i.e., after the laser pulse is finished, there is no significant vaporization anymore, and the vapor density at the target is rather low, but the vapor expands away from the target, as is visualized by the various curves at successive times. The expansion is much more pronounced at higher values of the laser irradiance, as is clear from comparing the x-axes of the figures at 3×10^8, 10^9 and 10^{10} W/cm^2. This is especially true for the case of 3×10^8 W/cm^2, because it is just at the onset of evaporation. Indeed, at 100 ns, the vapor plume has only expanded about 0.1 mm at a laser irradiance of 3×10^8 W/cm^2, whereas at 10^9 and 10^{10} W/cm^2, the vapor plume ranges till about 0.8 and 2 mm, respectively, after 100 ns.

The background He gas is initially, i.e., before the laser pulse, at 1 atm, which corresponds to a number density of 2.45×10^{25} m^{-3}. However, as soon as vaporization starts and the vapor expands, it pushes the background gas away from the target, leading to a depletion in density near the target, and a pile-up of gas density in front of the vapor plume, as is clear from Fig. 3b. The shock front, indicated by the significant drop in gas density back to undisturbed values, also moves away from the target, as time evolves, and moreover, it reaches further distances from the target, for higher values of laser irradiance. It is also remarkable that the He gas rises at the position where the Cu vapor density drops to very low values, so that there is almost no mixing between the Cu vapor and the He background gas.

The velocity distributions of the expanding plume are illustrated, at successive times, in Fig. 3c. The plume velocity increases away from the target, but drops suddenly to zero at the shock front. The maximum velocity is calculated in the order of 1000–1500 m/s, at the laser irradiance of 3×10^8 m/s, but it reaches values of 10,000 m/s and 20,000 m/s, at laser irradiance values of 10^9 and 10^{10} m/s, respectively. Finally, it should be noted that the velocity is calculated to be negative near the target. This indicates that there is a backward flux of the vapor plume onto the target, which can be responsible for splashing of the molten target material (not yet included in our model). Note, however, that a negative velocity during the laser pulse is a bit unexpected, in view of the strong evaporation occurring at the target surface. It is the result of the boundary condition imposed for the plume velocity (or flux), which is defined from the Hertz–Knudsen equation [18]:

$$J = \frac{P_s - P_g}{\sqrt{2\pi m k T_s}}$$

where J is the condensation flux, P_s and P_g stand for the saturated vapor pressure and gas pressure, respectively, and T_s is the target surface temperature. Hence, when the saturated vapor pressure becomes lower than the gas pressure, a negative flux, and hence velocity, is predicted. In principle, this can be possible, even when strong evaporation occurs, because of the high plume pressure. However, it might also be that this boundary condition is not appropriate for our problem, during the laser pulse. In the near future, we plan to investigate in more detail the effect of this boundary condition, because it might also influence the calculation of the surface temperature, as mentioned in Section 3.1.1.

The plume expansion velocity has been measured in several papers, for the range of laser irradiance studied here (10^9–10^{10} W/cm^2), and typical values in the order of 10000 m/s are indeed reported, increasing with laser irradiance [37,57–59]. The velocity also decreases gradually with time [37,59], in correspondence with our model predictions. Consequently, the corresponding plume dimensions are measured in the mm range after 100 ns, increasing with laser irradiance [30,59,60]. Similar results for the plume velocity and dimensions were also obtained from other simulation models [14,55,61,62]. Finally, it is also reported in literature that the plume velocity drops as a function of background gas pressure [63–65], and this is indeed also observed from our modeling results, if we compare the data in Fig. 3 (at 10^9 W/cm^2) with our calculation results for the same laser irradiance, presented in Ref. [10] for expansion in vacuum.

The temperature distributions in the expanding plume (figures (d)), show that the maximum temperature is reached at the maximum of the Cu vapor density, and that the temperature of the piled-up background gas is considerably lower. However, it is still clearly higher than the temperature of the undisturbed gas, which is fixed at 300 K. Further, it is obvious that the plume temperature is highest during the laser pulse, and drops gradually as a function of time. At a laser irradiance of 3×10^8 W/cm^2, the maximum temperature is only calculated to be around 1000–2000 K, which is too low for plasma formation, as will be demonstrated below. At 10^9 W/cm^2, the maximum temperature reaches

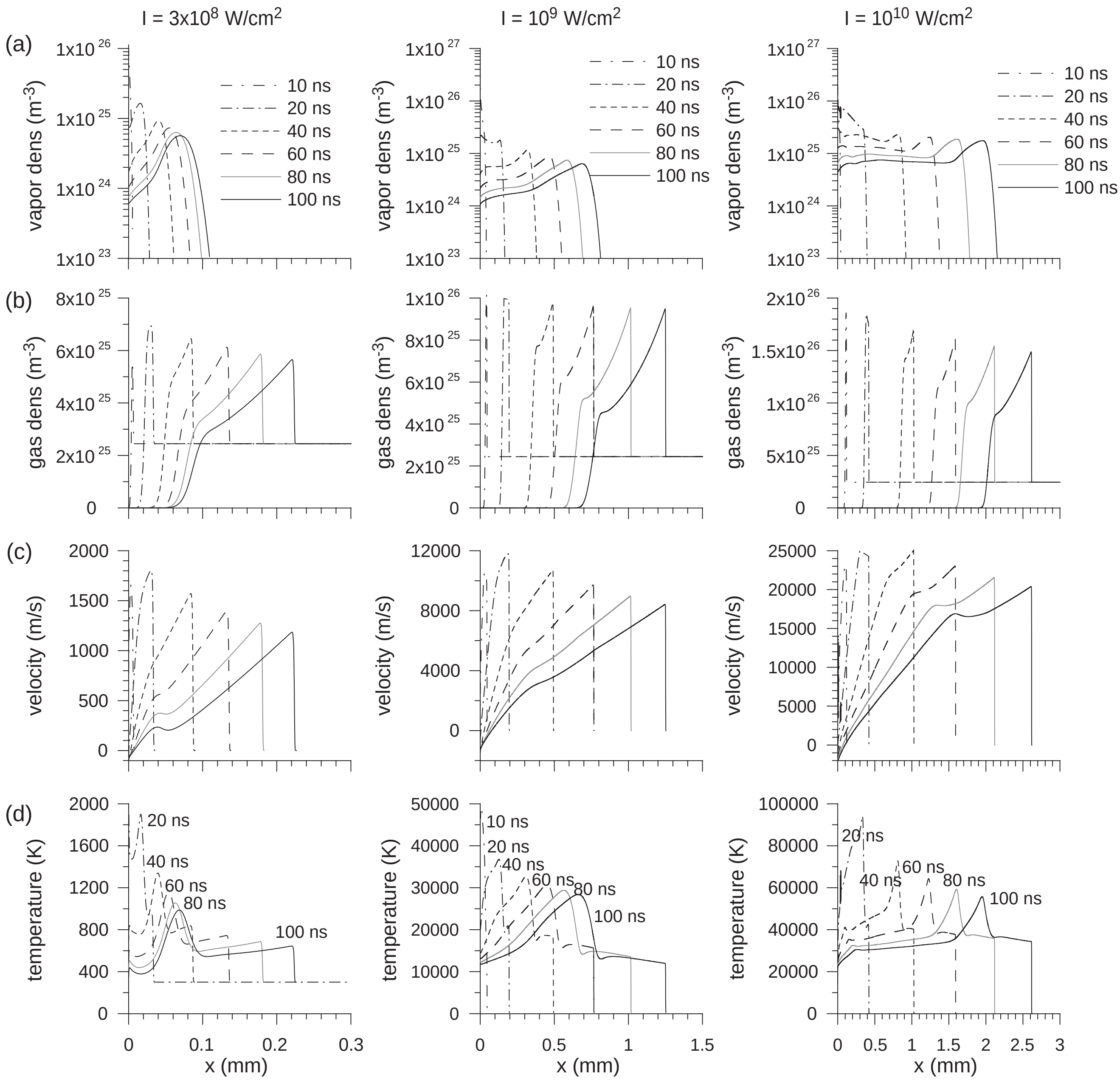

Fig. 3. Calculated spatial distributions in the plume of vapor density (a), background gas density (b), plume velocity (c) and plume temperature (d), at six different times between 10 and 100 ns, for laser radiation of 266 nm and 5 ns pulse duration, at a laser irradiance of 3×10^8 W/cm^2 (left set of figures), 10^9 W/cm^2 (middle set of figures), and 10^{10} W/cm^2 (right set of figures).

values of 30,000–50,000 K, and at 10^{10} W/cm^2, the calculated temperature could reach values of almost 100,000 K, although values of 30,000–40,000 K are more typical in the main portion of the plume.

Our calculated temperature values appear to be slightly higher than some experimental values reported in the literature, which are typically in the order of 10,000–40,000 K for the early stage (e.g., first 100 ns), in the laser irradiance range of 10^9–10^{10} W/cm^2 [22,23,49,58]. It is possible that our model overestimates the plume temperature to some extent, because some energy loss mechanisms are not yet included in the model, such as excitation (i.e., energy transfer into excited levels) and radial plume expansion (resulting in heat loss in the radial direction). However, it should also be realized that the above papers do not always clearly point out at which position in the plume the temperature values are measured, and it follows from Fig. 3 that the plume temperature varies greatly as a function of position in the plume. This is also observed in Ref. [46] where the measured plume temperature increases from 11,000–16,000 K near the target, up to 60,000 K at 1 mm from the target, for a laser irradiance of 10^{10} W/cm^2 at 355 nm. Hence, these data are in very good agreement with our calculated results. Moreover, it should be mentioned that there are also some papers, which report on higher temperature values than our calculated data. For instance, in Ref. [36,66] a temperature of about 25,000 K was obtained, for a laser irradiance of 5×10^8 W/cm^2, and in Ref. [37] a temperature of 400,000 K was reported for a laser irradiance of 4.6×10^{10} W/cm^2, with a 10 ns pulse at 532 and 1064 nm, and glass samples.

At such high calculated temperature values for 10^9 and 10^{10} W/cm^2, as illustrated in Fig. 3, ionization of the vapor and background gas, and hence plasma formation, certainly takes place. In Fig. 4, the calculated fractions of Cu^0 and He^0 atoms, and Cu^+, Cu^{2+} and He^+ ions, are plotted as a function of position in the plume, at four different times (a–d), and at three different values of laser irradiance. Note that the sum of the Cu^0, Cu^+ and Cu^{2+} fractions is always equal to one, as is also the case for the sum of the He^0 and He^+ fractions. Also shown are the corresponding calculated temperature profiles for these conditions, in order to facilitate the explanation of the ionization fractions.

The upper set of figures illustrates the results at a laser irradiance of 5×10^8 W/cm^2, which is just above the threshold for plasma formation. Indeed, at 3×10^8 W/cm^2, no plasma formation was observed yet. It appears that at 5×10^8 W/cm^2 the He gas is still mainly in atomic form, because it is characterized by a rather high ionization potential of 24.58 eV, but the Cu vapor is almost fully ionized into Cu^+ ions. Note that the first ionization potential of Cu is, indeed, only 7.73 eV, whereas the second ionization potential is equal to 20.29 eV. At 10 ns (i.e., during the laser pulse), 20% of the Cu vapor is even doubly ionized near the target, where the plume temperature reaches values of 35,000 K. As time evolves, the plume temperature drops gradually, and the Cu^{2+} ions recombine again with electrons into Cu^+ ions and further into Cu^0 atoms. However, even at 100 ns, the Cu vapor still consists mainly of Cu^+ ions in most of the vapor plume.

At the laser irradiance of 10^9 W/cm^2 (middle set of figures), the plume temperature was calculated to rise till almost 50,000 K during the laser pulse (i.e., at 10 ns), which results in a significant amount of ionization. Indeed, the Cu vapor is found to be mainly ionized into Cu^{2+} ions, and the atomic fraction is nearly negligible. In certain regions of the plume, it was found that the He gas was even ionized for about 40%. Note, however, that in this region of the plume, the background gas has a low density (see Fig. 3), so that the He^+ ion density is in fact still very low. At later times, the plume temperature is somewhat lower, and the He ionization drops, but the Cu vapor remains ionized (mainly in the form of Cu^+ ions) for a long time after laser pulse termination, as can be deduced from the plot at 100 ns.

Finally, at the laser irradiance of 10^{10} W/cm^2 (lower set of figures), the ionization of Cu and He is even more extreme. Indeed, it was calculated that at 10 ns the He gas is fully ionized into He^+ ions, and the Cu vapor is fully ionized into Cu^{2+} ions. It should be mentioned that we have only taken into account first order ionization of He, and first and second order ionization of Cu, but at these extreme situations, it is very probable that He is further ionized into He^{2+} ions, and the Cu vapor may also exist in the form of Cu^{3+} ions. Note also that the calculated ionization fractions near the target show some oscillations, which are due to spikes in the temperature profile. The latter are attributed to an instability in the calculations at such high values of laser irradiance, due to the critical influence of the boundary conditions, and the fact that the interaction between target and plasma is also unstable (i.e., far from equilibrium) in reality, during the short time of the laser pulse. However, this instability occurs only during and shortly after the laser pulse, and does not affect the further calculations. It is clear that at this high laser irradiance, the ionization of Cu and He lasts for a relatively long time after the laser pulse is finished, and at 100 ns, the Cu^{2+} ions and He^+ ions still constitute the major fraction of the Cu vapor and He gas, respectively, in a certain part of the plume, where the temperature is at its maximum.

Such high ionization degrees are also reported in the literature. For instance, Russo et al. measured the ratio of ion to atom number densities, for a Nd:YAG laser at 266 nm and 3 ns pulse duration, in the laser irradiance range of 2×10^9–2×10^{10} W/cm^2, and they obtained values in the range of 0.3 to 300, increasing with $I^{2.07}$, which corresponds to an ionization degree of 30% to full ionization [23]. Capitelli et al. reported on a ratio of Ti^+ ion number density over Ti^0 atom number density in the order of 150, at 200 ns, for a laser pulse of 5 J/cm^2 and 30 ns pulse duration [65]. Finally, in Ref. [58] the presence of multiply charged ions is demonstrated, based on spectral lines, for a laser irradiance of 10^{10} W/cm^2.

Fig. 5 presents the calculated density profiles of the various species in the plume, at different times, either during the laser pulse (i.e., at 10 ns) as well as after laser–solid interaction (at 20, 40 and 100 ns), for the same irradiance values as in previous figures. Note the change in the x-axis going from Fig. 5a to d. At 10 ns (Fig. 5a) the Cu vapor is at maximum adjacent to the target, as was also clear from Fig. 3. At a laser irradiance of 5×10^8 W/cm^2, it consists mainly of Cu^+ ions. At 10^9 W/cm^2, the Cu^+ and Cu^{2+} ions are equally important, and at 10^{10} W/cm^2, the Cu^{2+} ions are the most abundant Cu species. The He gas is pushed away from the target, but at 10 ns, it has a lower density than the Cu vapor (see right y-axes in Fig. 5a), and it is practically not ionized. Hence, the electron density (which is equal to the sum of the densities of Cu^+ and He^+ ions and twice the Cu^{2+} ion density) is fully determined by the Cu^+ and Cu^{2+} ions, and it is characterized by a maximum near the target (see the thicker black solid line). At 10 ns, i.e., during the laser pulse, the maximum electron density was calculated to be almost 2×10^{26} m^{-3} at 5×10^8 W/cm^2, about 5×10^{26} m^{-3} at 10^9 W/cm^2, and nearly 3×10^{27} m^{-3} at 10^{10} W/cm^2, but the densities drop drastically further away from the target, and they are also significantly lower after termination of the laser pulse (see further).

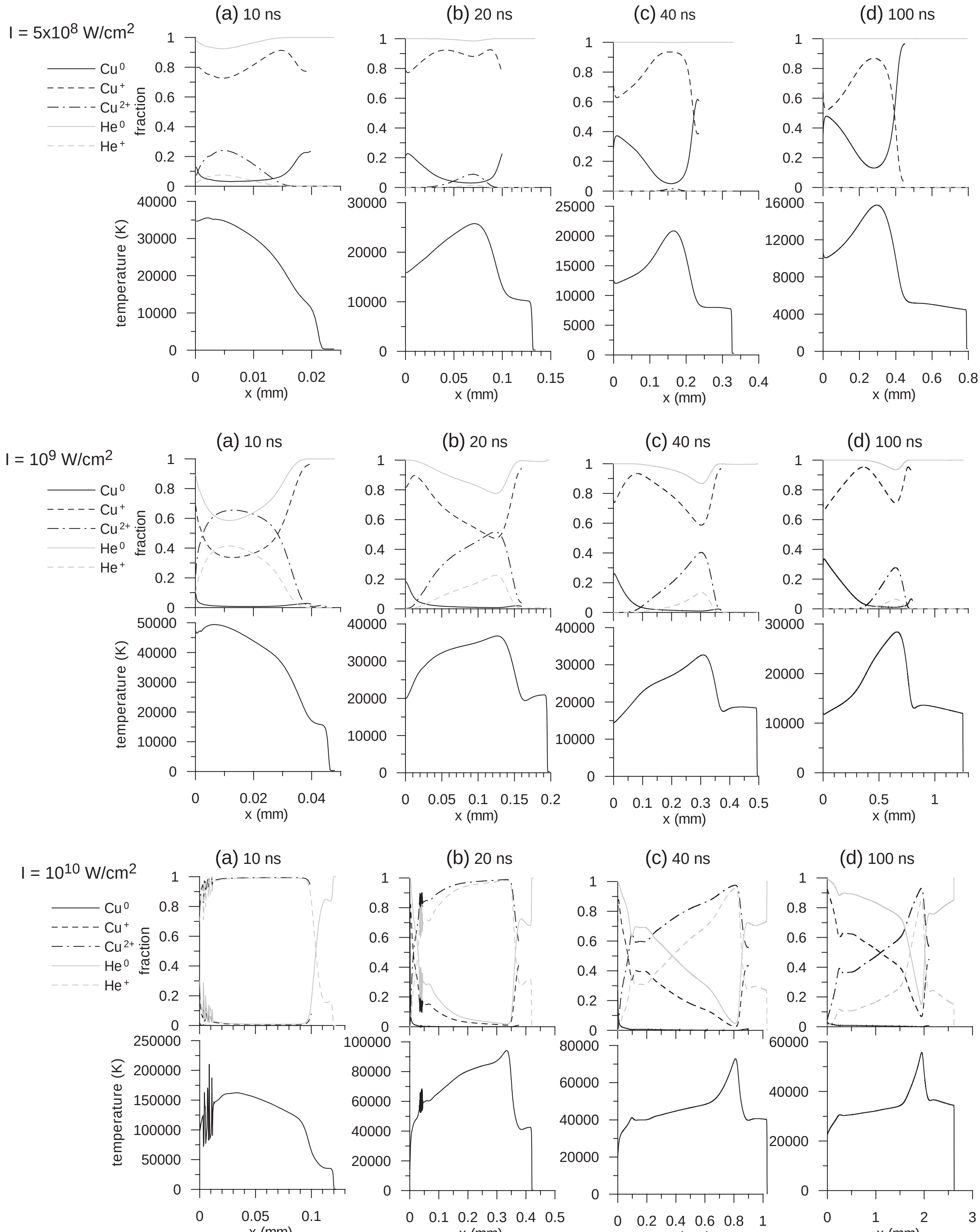

Fig. 4. Calculated spatial distributions of the ionization fractions of Cu (black lines) and He (grey lines) in the plume, as well as the corresponding plume temperature distributions, at four different times between 10 and 100 ns, for laser radiation of 266 nm and 5 ns pulse duration, at a laser irradiance of 5×10^8 W/cm^2 (upper set of figures), 10^9 W/cm^2 (middle set of figures), and 10^{10} W/cm^2 (lower set of figures).

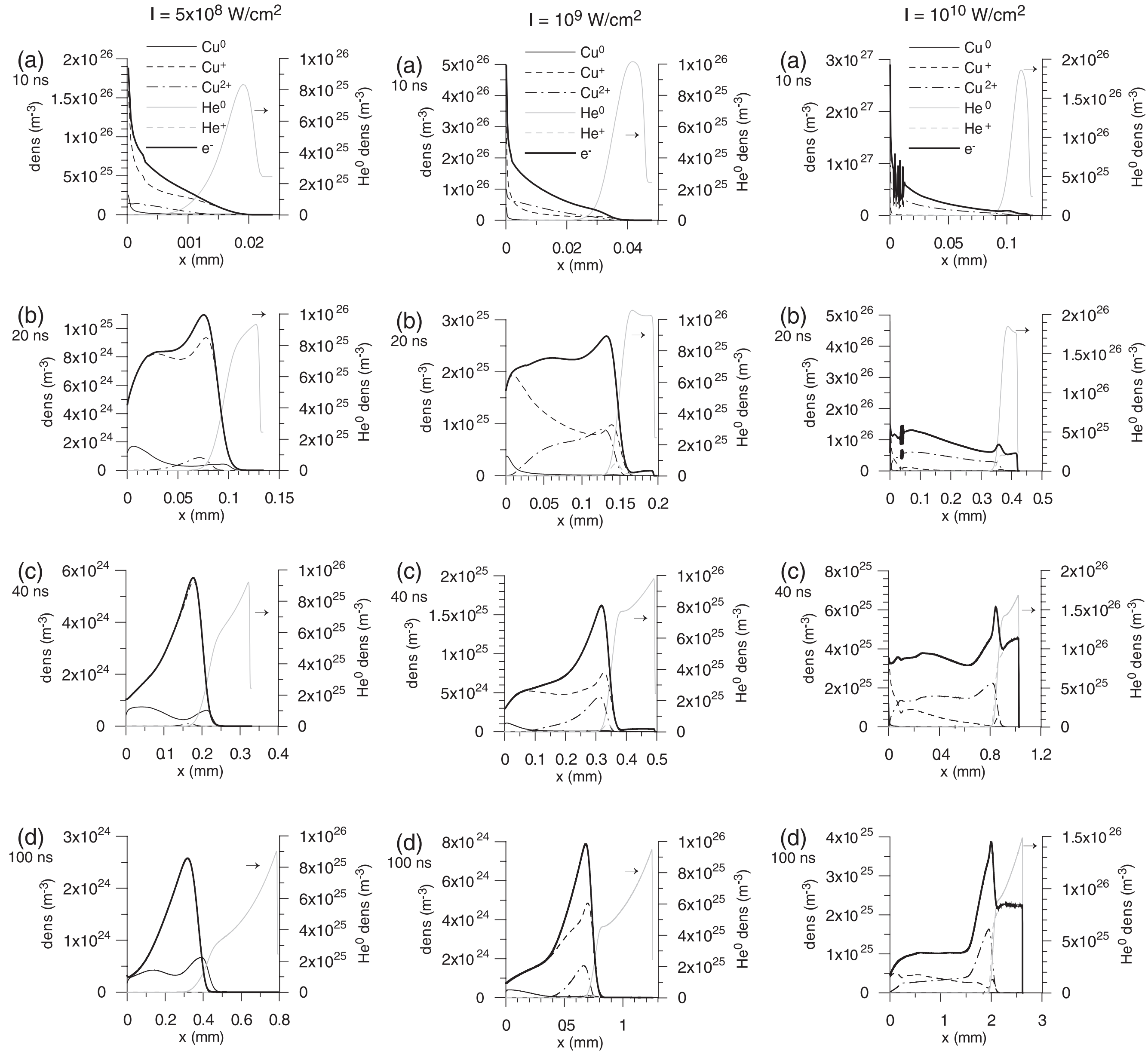

Fig. 5. Calculated spatial distributions of the number densities of Cu atoms and ions (black lines), He atoms and ions (grey lines) and electrons (thick solid lines) in the plume, at four different times between 10 and 100 ns, for laser radiation of 266 nm and 5 ns pulse duration, at a laser irradiance of 5×10^{8} W/cm^2 (left set of figures), 10^{9} W/cm^2 (middle set of figures), and 10^{10} W/cm^2 (right set of figures). Note that the He atom number densities are represented by the right *y*-axes, because of the different orders of magnitude.

At later times, when vaporization has ceased, the maximum Cu vapor density is shifted away from the target due to plume expansion, and this applies also to the Cu^+ and Cu^{2+} ion densities, and hence to the electron density profiles. Moreover, the maximum densities of Cu vapor, Cu^+ and Cu^{2+} ions, and electrons, are significantly reduced, because the plume is more spread out. At 20 ns (Fig. 5b), the density of Cu is already lower than the He background gas density (cfr. the left and right *y*-axes), and this trend continues for later times. At 5×10^{8} W/cm^2, the electron density profile is almost equal to the Cu^+ ion density profile, and the calculated maximum density drops from 10^{25} m^{-3} at 20 ns, to 6×10^{24} m^{-3} at 40 ns, and 2.5×10^{24} m^{-3} at 100 ns. At 10^{9} W/cm^2, the electron density is more or less equal to the sum of the Cu^+ ion density and twice the Cu^{2+} ion density, and the maximum density drops from 2.5×10^{25} m^{-3} at 20 ns, to 1.5×10^{25} m^{-3} at 40 ns, and almost 8×10^{24} m^{-3} at 100 ns. At 10^{10} W/cm^2, the electron density profile is equal to twice the Cu^{2+} ion density in the region of the vapor plume, and it is equal to the He^+ ion density in the region in front of the vapor plume, where the He background gas is piled up. At such high laser irradiance, our model predicts that the electron density reaches values as high as 10^{26} m^{-3} at 20 ns, $3–6\times10^{25}$

m^{-3} at 40 ns, and 10^{25} m^{-3} (with a maximum of 4×10^{25} m^{-3}) at 100 ns.

Several papers have focused in recent years on measuring the electron density in the laser-induced plasma. However, they often report on measurements in the μs-regime [58,67–71], for which our model is not yet applicable. There are still a number of papers, which do present measurements in the first 100 ns, so that comparison is possible. Most of these papers, however, show density values in the range of 7×10^{17}–7×10^{18} cm^{-3} (or 7×10^{23}–7×10^{24} m^{-3}) for a laser irradiance in the order of 4×10^{8}–10^{10} W/cm^2 [22,23,47,57,65,66], hence somewhat lower than our presented calculation results. This is probably attributed to the fact that the plume temperature is somewhat overestimated in our model, because certain, possibly relevant energy loss mechanisms are not yet included in the model (see above). Nevertheless, in Ref. [25] electron number density values are presented in the order of $1-8\times10^{24}$ m^{-3}, depending on position in the plume, for a laser irradiance of 3×10^{8} W/cm^2 [25]. This value of laser irradiance is just below the threshold for plasma formation in our model, so that our model predicts the electron density to be roughly zero for these conditions. Of course, exact comparison is not possible, since the experiments were carried out in vacuum, for a Mg target and a laser wavelength of 248 nm, but it shows that relatively high values of electron number density have been reported in the literature, even for rather low values of laser irradiance. Moreover, in Ref. [37] relatively high electron number densities of about $2-6\times10^{25}$ m^{-3} were achieved for a Nd:YAG laser of 532 and 1064 nm with 10 ns pulse duration, at a laser irradiance of 4.6×10^{10} W/cm^2. Finally, in Ref. [36] the electron density was found to be about 7×10^{26} m^{-3} for a laser irradiance of 5×10^{8} W/cm^2, and about 3×10^{27} m^{-3} at 5×10^{10} W/cm^2, for an excimer laser of 248 nm and 10 ns pulse duration, which is even higher than our calculated results.

Fig. 6 illustrates the influence of the laser irradiance on several plume characteristics, all calculated at 100 ns. The maximum Cu vapor density (Fig. 6a) rises as a function of laser irradiance, which is attributed to the increased target vaporization. The maximum He gas density (Fig. 6b) shows the same trend, which is logical, because more Cu vapor can push the background gas to a larger pile-up. Comparing Fig. 6a and b shows that the maximum He density is typically about one order of magnitude higher than the maximum Cu vapor density, at 100 ns (i.e., in the order of 10^{26} m^{-3} vs. 10^{25} m^{-3}). The plume velocity also increases with laser irradiance, as is clear from Fig. 6c, and this is due to the higher surface temperature. The maximum plume velocity at 100 ns is typically calculated in the order of 5000–20,000 m/s, which is in good agreement with data reported in the literature (see above). Because of this higher plume velocity, the plume length after 100 ns (Fig. 6d) is also larger at higher laser irradiance, as well as the length of the shock

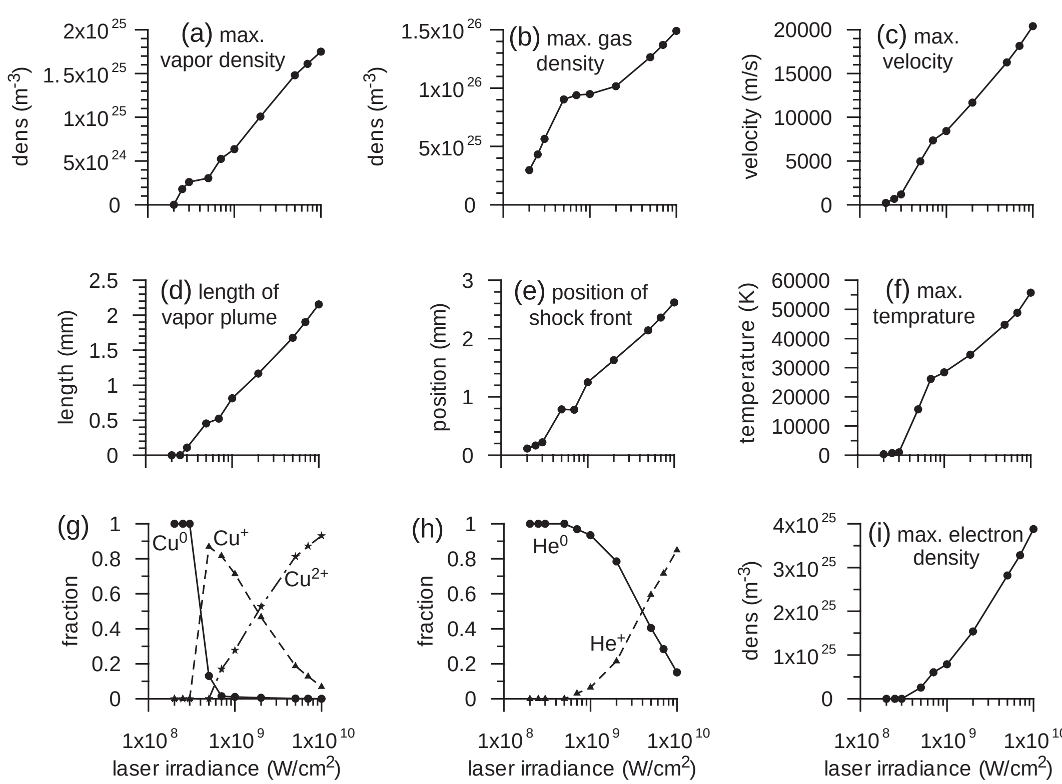

Fig. 6. Calculated maximum vapor number density (a), maximum background gas number density (b), maximum plume velocity (c), length of the vapor plume (d), shock front position (e), maximum temperature (f), fraction of Cu^0 atoms, Cu^+ and Cu^{2+} ions (g), fraction of He^0 atoms and He^+ ions (h), and maximum electron number density in the plume (i), all at 100 ns, as a function of laser irradiance, for laser radiation of 266 nm and 5 ns pulse duration.

front (Fig. 6e), i.e., the position where the background He density drops again to the undisturbed values corresponding at 1 atm. The calculated vapor plume length at 100 ns is in the order of a few mm, and the position of the shock front is only slightly further away (typically 0.4–0.5 mm, which corresponds to the region of the background gas pile-up). The maximum temperature in the plume (Fig. 6f) increases also with laser irradiance, and this is connected to the rise in electron density (Fig. 6i). Indeed, a higher plume (plasma) temperature yields more ionization, and hence a higher electron density, and vice versa, a higher electron density leads to more laser absorption in the plasma, by inverse Bremsstrahlung (IB, see further), and consequently to a higher plasma temperature. The plume temperature and electron density are equal to 300 K and zero, respectively, for a laser irradiance below or equal to 3×10^{8} W/cm^2, which indicates that no plasma is formed yet. However, for a laser irradiance above this threshold, the maximum plasma temperature is in the range of 20,000–50,000 K, and the maximum electron density at 100 ns is calculated in the order of 2.5×10^{24}–4×10^{25} m^{-3}, for a laser irradiance ranging from 5×10^{8} till 10^{10} W/cm^2. This plasma ignition threshold in the order of 3×10^{8} W/cm^2 is in excellent correspondence with the values reported by Russo's group, for similar laser conditions [23,26,31]. From the data in Fig. 6f and i, it could be deduced that the temperature and electron density, above 5×10^{8} W/cm^2, vary with laser irradiance as $T\sim I^{0.3}$, and $N_e\sim I^{0.5}$. Mao et al. and Liu et al. reported the following power laws below a laser irradiance of 2×10^{10} W/cm^2: $T\sim I^{0.14}$ and $N_e\sim I^{0.32}$ in Ref. [22] and $T\sim I^{0.54}$ and $N_e\sim I^{0.24}$ in Ref. [23]. Hence, the dependence of electron density as predicted in our model, is somewhat overestimated, compared to the experiment. The calculated dependence of plume temperature, on the other hand, falls in between the two dependencies reported experimentally. In general, it can be concluded that the effect of laser irradiance is realistically predicted with our model.

Related to the behavior of plume temperature as a function of laser irradiance are the calculated ionization fractions of Cu and He, which are depicted in Fig. 6g and h, respectively. At a laser irradiance below or equal to 3×10^{8} W/cm^2, no plasma is formed, and the Cu vapor and He gas are not ionized. As soon as plasma ignition occurs, the fraction of Cu^0 atoms will suddenly drop, to only 10% of the total Cu vapor at about 5×10^{8} W/cm^2, whereas the Cu^+ fraction is almost 90%. At increasing laser irradiance, the Cu^0 fraction will soon become negligible, and the Cu^+ fraction will gradually decrease, whereas the Cu^{2+} fraction becomes predominant. The He^0 fraction also drops for increasing laser irradiance, but it becomes only lower than the He^+ fraction at a laser irradiance above 3×10^{9} W/cm^2, which is due to the higher ionization potential of He (see above).

We have also plotted the maximum plume temperature, the maximum electron density, and the shock front position at 100 ns, as a function of time during and after the laser pulse, and the result is shown in Fig. 7 (a–c), for different values of laser irradiance. The symbols represent the calculated results, whereas the solid lines indicate some fitted curves, as given in the legend. Note that the calculated electron density values at 10 ns are not included in Fig. 7b, because these values are significantly higher, because of the additional thermionic emission from the target during the laser pulse (see also Fig. 5), and including these data would make the figure less clear, because the curves would all come closer to each other. It is clear from Fig. 7a and b that

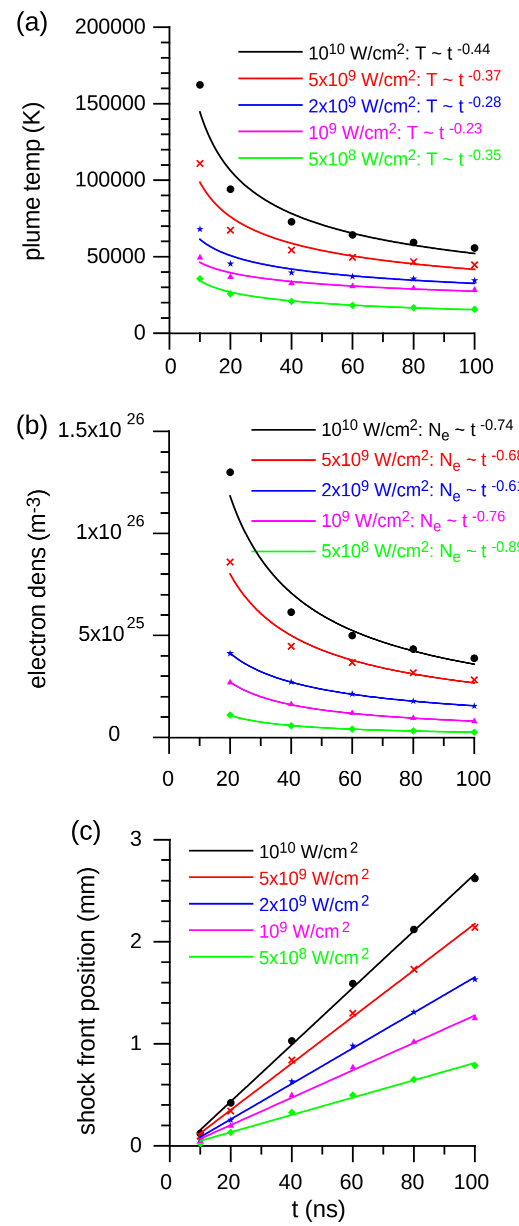

Fig. 7. Calculated maximum values of plume temperature (a) and electron number density (b), and calculated shock front position (c), as a function of time up to 100 ns, for laser radiation of 266 nm and 5 ns pulse duration, at different values of laser irradiance. The symbols stand for the calculated data, whereas the solid lines represent some fitted curves, as indicated in the figure legends.

the plume temperature and electron density both drop as a function of time, and the time-behavior can be fitted with a power law: $T \sim t^{-n}$ and $N_e \sim t^{-m}$, where $n \sim 0.23-0.44$, and $m \sim 0.6-0.9$, for the different values of laser irradiance. This is slightly lower than the fits given in the papers of Russo's group for a Nd:YAG laser at 266 nm and 3 ns pulse duration, i.e., $T \sim t^{-0.54}$ and $N_e \sim t^{-0.95}$ for a laser irradiance of 7.6×10^9 W/cm^2 on glass samples [22] and $T \sim t^{-0.7}$ and $N_e \sim t^{-0.99}$ at 4.6×10^{10} W/cm^2 on Si samples [23]. However, an exact comparison is not straightforward, because the conditions are slightly different. Moreover, it is not clear at which position the measurements were performed, and it is well possible that the maximum temperature and electron density, as plotted in our Fig. 7, will exhibit a somewhat different time behavior than values taken at another position in the plume. Nevertheless, the values appear to be in the same order, so the general time behavior of plume temperature and electron density appears to be correctly predicted by the model.

Finally, the position of the shock front increases linearly with time, as appears from Fig. 7c. This is because of the forward expansion, which is considered in our one-dimensional model. In Ref. [60] the measured plasma length was found to increase with time according to a power law: $z \sim t^{0.76}$ during the laser pulse, and $z \sim t^{0.44}$ after termination of the laser pulse, for a Nd:YAG laser at 1064 nm, 15 ns pulse duration and 40 mJ energy, for metallic samples and expansion in air at 1 atm. It is stated in this paper that this time behavior is typical for spherical expansion after the laser pulse, so it appears that our one-dimensional model is somewhat overestimating the plume expansion dynamics. In the near future, we will extend our model to include spherical expansion. However, it should also be realized that the experiments in Ref. [60] were carried out in air, and it is expected that the expansion in heavier gases, like air, will be somewhat slower than in He, as will be investigated in detail in a separate paper [72].

3.1.3. Laser absorption in the plasma

As mentioned above, once a plasma is formed, part of the laser beam will be absorbed in the plasma, by electron–ion or electron–neutral inverse Bremsstrahlung (e–i IB and e–n IB), or by photo-ionization (PI). Consequently, not the full laser irradiance will be able to reach the target, which is called "plasma shielding". Fig. 8 illustrates the laser irradiance time-profiles for different values of laser irradiance (solid lines), as well as the time-profiles of the laser irradiance arriving at the target, i.e., after passage through the plasma (dashed lines). For a laser irradiance of 3×10^8 W/cm^2 and lower, no plasma formation, and hence no absorption of the laser beam, takes place, and the laser irradiance arriving at the target is exactly the same as the irradiance emitted by the laser. Hence, the laser irradiance time-profiles of these conditions are not presented in Fig. 8. However, for higher laser irradiance, plasma formation and laser beam absorption do take place, so that the laser irradiance reaching the target is lower than the original laser irradiance. It is clear from Fig. 8 that the laser absorption increases with rising laser irradiance, because of the higher electron and neutral densities in the plume, which are responsible for the absorption processes (see above). The percentage absorption increases drastically with laser irradiance, up to a value of 80% at 10^{10} W/cm^2, as is illustrated in Fig. 9a. This behavior corresponds reasonably with Ref. [57], where it is reported that the plasma transmission during or shortly after the laser pulse is about 10–20%, for a Nd:YAG laser of 1064 nm, 10 ns pulse duration and 275 mJ energy, and expansion in air at 1 atm. Moreover, Shannon et al. and Chan and Russo [26,31] have demonstrated that the emission signal intensities from ICP-AES increase with laser irradiance, but the slope is higher below a certain threshold than above this value. This so-called roll-off of the emission intensity at a certain laser irradiance is also attributed to plasma shielding. This process of laser absorption is found to become significant for a laser irradiance above 10^9 W/cm^2, as reported in Ref. [31] and above a value in the range of $1-3 \times 10^8$ W/cm^2, as presented in Ref. [26]. Similarly, the mass ablation rate of Cu was found to increase with laser irradiance, according to a power law, where the value of the exponent was in the order of 2–5 for a laser irradiance below 3×10^8 W/cm^2, and it was smaller than 1, for a laser irradiance above this value [24]. This is also attributed to plasma shielding, which comes into play for laser irradiance values above 3×10^8 W/cm^2 [24]. Hence, the threshold value predicted with our model (i.e., between 3×10^8 and 5×10^8 W/cm^2) is in the same order as in the experiments [24,26,31], so that we can conclude that our model yields a more or less realistic description of the plasma behavior.

Fig. 10 shows the computed absorption coefficients of the three different absorption mechanisms taken into account in the model, for different values of the laser irradiance, at 10 ns. IB involves the absorption of a photon by a free electron, in which the electron is raised to a higher state in the continuum. This process must occur within the field of a heavy particle (ion or neutral), so that momentum is conserved [73]. The electron–neutral and electron–ion IB absorption coefficients are calculated as [74]:

$$\alpha_{\mathrm{IB,e-n}} = \left[1 - \exp\left(-\frac{hc}{\lambda kT}\right)\right] N_e (Q_{\mathrm{e-Cu}} N_{\mathrm{Cu}^0} + Q_{\mathrm{e-He}} N_{\mathrm{He}^0}) \tag{1}$$

$$\alpha_{\mathrm{IB,e-i}} = \left[1 - \exp\left(-\frac{hc}{\lambda kT}\right)\right] \frac{4e^6 \lambda^3 N_e}{3hc^4 m_e} \left(\frac{2\pi}{3 m_e kT}\right)^{1/2} \times (N_{\mathrm{Cu}^+} + 4N_{\mathrm{Cu}^{2+}} + N_{\mathrm{He}^+}) \tag{2}$$

where λ is the laser wavelength, N_e is the electron number density, T is the plume temperature, N_{Cu^0}, N_{Cu^+}, $N_{\mathrm{Cu}^{2+}}$, N_{He^0} and N_{He^+} represent the Cu^0, Cu^+, Cu^{2+}, He^0 and He^+ ion densities, respectively, Q is the cross section of photon

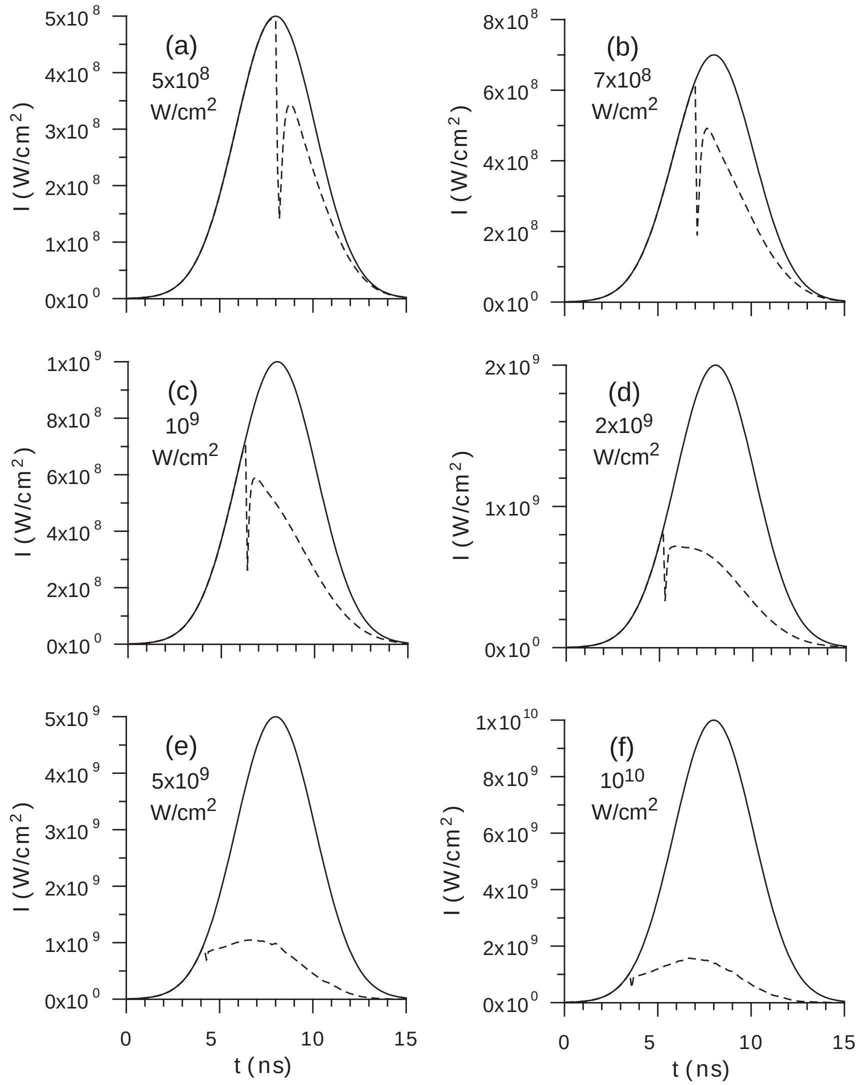

Fig. 8. Laser irradiance–time profiles, for a laser of 266 nm and 5 ns pulse duration, at different values of laser irradiance (solid lines), as well as the calculated values of actual laser irradiance reaching the target, i.e., after passing through the plasma (dashed lines).

absorption (assumed as 10^{-46} m^5 for Cu, and 2×10^{-48} m^5 for He [74,75]) and the other symbols are self-explanatory.

The third absorption mechanism is photo-ionization (PI) of excited atoms. Atoms in excited levels are not yet explicitly included in our model, but we calculate their relative population, based on the Boltzmann distribution of statistical thermodynamics theory:

$$p_i = \frac{N_i}{N_{\mathrm{tot}}} = \frac{g_i \exp(-E_i/kT)}{\sum_j g_j \exp\left(-E_j/kT\right)}$$

where p_i and N_i stand for the relative and absolute population density of level i, N_{tot} is the total population density of all levels, g_i and E_i represent the statistical weight and excitation energy of level i, and T is the plasma temperature. The PI absorption coefficient is approximated as $\sigma_{\mathrm{PI}}N_{\mathrm{Cu}}$, where N_{Cu} is the Cu vapor atom density and σ_{PI} is estimated based on a constant value of 1.5×10^{-21} m^2, as found in literature [53,76], but corrected for the availability of excited levels lying close enough to the ionization limit (based on the relative populations as calculated above), so that the energy difference is smaller than the energy of the laser photons. Hence, it is obvious that a higher plume temperature yields a higher relative population of highly excited levels, resulting in a higher probability of photo-ionization.

It is clear from Fig. 10 that laser beam absorption by the three different mechanisms, and hence the overall plasma shielding, is especially important near the target, where the Cu vapor, ion and electron densities reach their maximum (see Fig. 5 above). This corresponds with Ref. [23] where it is stated that most of the laser absorption takes place in the vapor layer confined close to the target surface. At a laser irradiance of 5×10^8 W/cm^2, e–n IB makes up clearly the dominant absorption mechanism, followed by PI, whereas

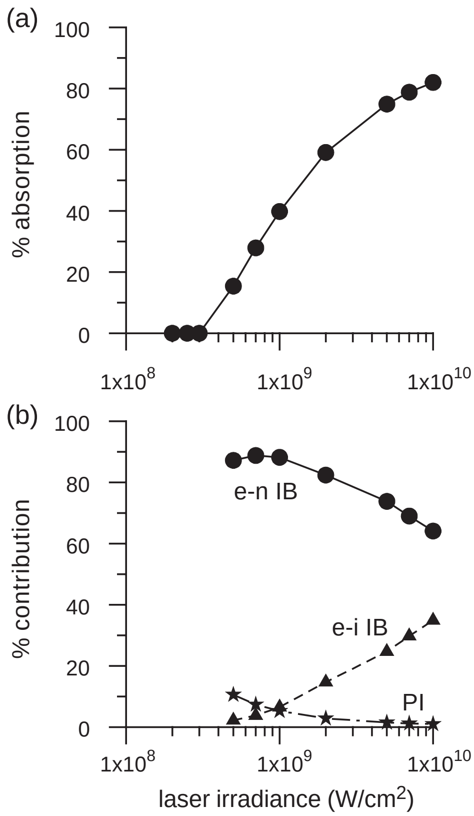

Fig. 9. Calculated relative amount of laser absorption in the plasma (a), and calculated relative contributions of electron–neutral and electron–ion inverse Bremstrahlung (e–n IB and e–i IB) and photo-ionization (PI) as absorption mechanisms (b), as a function of laser irradiance, for a laser of 266 nm and 5 ns pulse duration.

e–i IB is of minor importance. At higher laser irradiance, however, the ionization degree rises drastically, and consequently, e–i IB becomes gradually more important. This is also apparent from Fig. 9b, where it is shown that the relative contribution of e–i IB increases from a few % at 5×10^8 W/cm^2 to almost 40% at 10^{10} W/cm^2, whereas the relative contribution of e–n IB and PI drop with laser irradiance. However, our calculations predict that e–n IB always remains the dominant laser absorption mechanism, with a relative contribution ranging from almost 90% at low values of laser irradiance to about 60% at the highest laser irradiance investigated. This agrees not exactly with observations made by Liu et al. where it is stated that e–i IB becomes eventually the dominant laser absorption mechanism [23]. The reason for this dominant role of e–n IB, as predicted by our model, is that it appears especially important in the layer adjacent to the target, where the vapor density is extremely high, as is confirmed also in Ref. [23]. Nevertheless, it is also possible that e–n IB is somewhat overestimated in our model, because the absorption coefficient, and more specifically the value of the photon absorption cross section (symbol Q in the above formula), is subject to large uncertainties. The general tendency of the relative importance of the different absorption mechanisms,

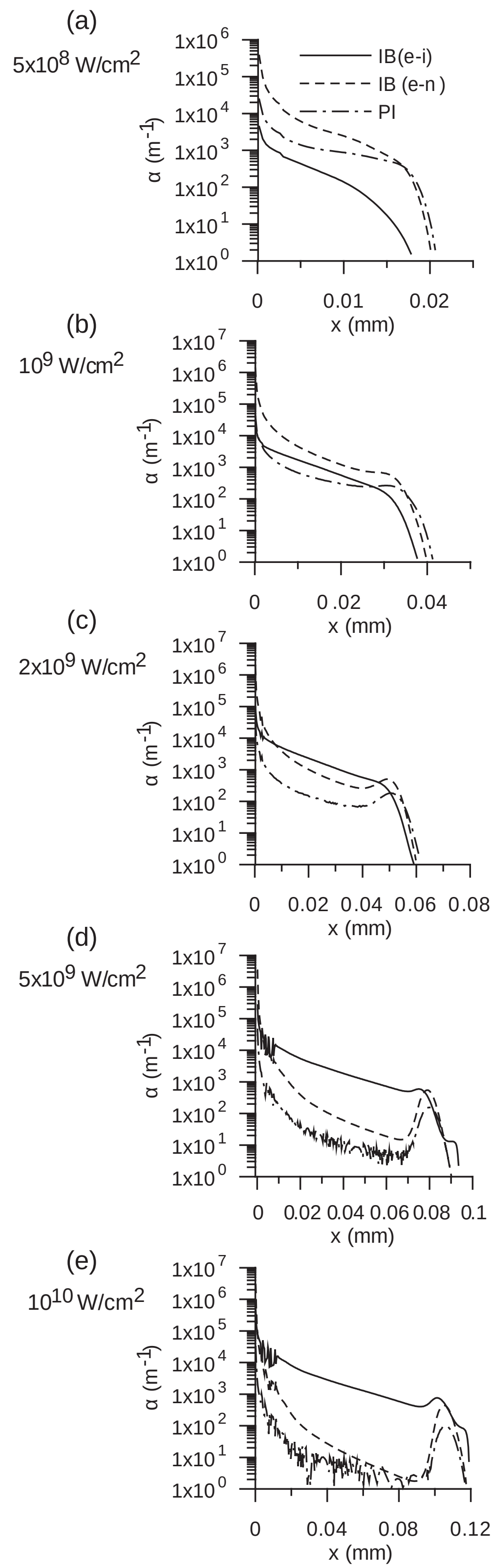

Fig. 10. Calculated absorption coefficients of e–i IB, e–n IB and PI, as a function of position in the plume, at 10 ns, for laser radiation of 266 nm and 5 ns pulse duration, at different values of laser irradiance.

as well as the overall amount of laser absorption, however, seem to be more or less correctly predicted with our model.

3.2. Effect of laser pulse duration

We have also investigated the effect of laser pulse duration on the target and plume (plasma) behavior, for a laser wavelength of 266 nm. In first instance, we have kept the laser irradiance fixed at 10^9 W/cm^2. It is clear that the laser fluence, which is defined as the laser irradiance integrated over the entire pulse, then increases with pulse duration, and consequently, this will affect the target and plume characteristics. In Fig. 11a, the laser fluence is plotted as a function of pulse duration, for the laser irradiance of 10^9 W/cm^2. It increases from 0.32 to 32 J/cm^2 for laser pulses in the range of 0.3–30 ns. In another series of runs, we have investigated the effect of pulse duration, keeping the laser fluence fixed at 10.6 J/cm^2, so that the laser irradiance varies from 10^{10} to 3.3×10^8 W/cm^2 for laser pulses ranging from 1 till 30 ns, as is shown in Fig. 11b.

Note that the laser pulse duration was varied between 0.3 and 30 ns. At shorter pulses, the laser fluence was too low (at fixed laser irradiance) for a plasma to be formed, or the laser irradiance was very high (at the same laser fluence). Moreover, other phenomena can start to take place at ps-laser pulses, such as the formation of an early-stage plasma by electron emission [77–79], which are not yet included in our model. Furthermore, the application of a one-temperature model (i.e., heat conduction equation) for the target also becomes questionable at very short (ps and fs) laser pulses, where the laser energy will not instantaneously be turned into heat, but into electron energy, so that the coupling of the electron and lattice temperature would need to be considered (i.e., in a two-temperature model) [80–83]. Longer pulses than 30 ns, on the other hand, are probably not of interest for practical use in LA and LIBS.

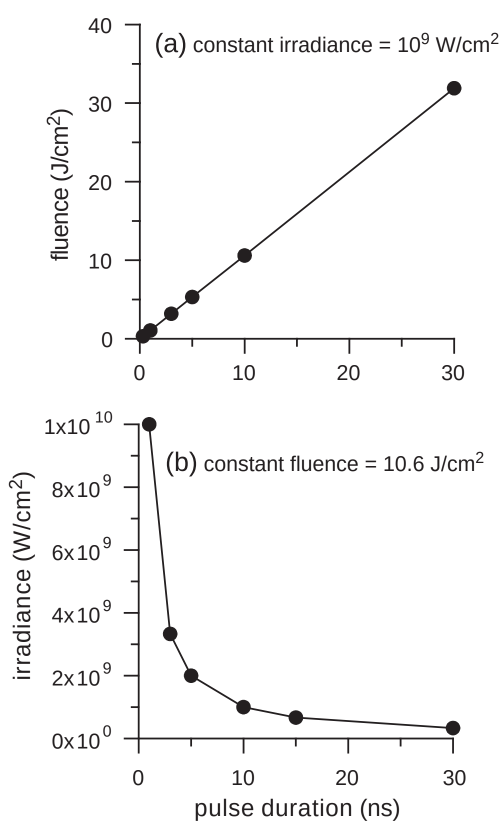

Fig. 11. Laser fluence as a function of laser pulse duration, for a fixed value of laser irradiance of 10^9 W/cm^2 (a), and laser irradiance as a function of pulse duration, for a constant laser fluence of 10.6 J/cm^2 (b).

3.2.1. Target heating, melting and vaporization

The calculated temperature distributions inside the target as a function of time (cf. Fig. 1) look very similar for different pulse durations, at least qualitatively, and they resemble Fig. 1; hence, they are not presented here. Instead, the maximum calculated surface temperature, maximum melt depth, maximum evaporation rate and total evaporation depth are plotted as a function of pulse duration, in Fig. 12, when keeping the laser irradiance or the laser fluence constant (part a and b, respectively).

It appears from Fig. 12a that the maximum surface temperature, as well as the maximum melt depth and total evaporation depth increase with pulse duration, at fixed laser irradiance, because the laser fluence, and hence the total laser energy reaching the target, increases. The surface temperature, however, reaches saturation at a pulse duration above 5 ns, and this can be explained by increased plasma shielding (see below), which compensates for the higher laser fluence. Also the maximum melt depth increases less than linearly, for the same reason. As far as evaporation is concerned, the 0.3 ns pulse seems to be too short for evaporation to take place, at the laser irradiance of 10^9 W/cm^2. Indeed, the maximum surface temperature is calculated to be only 4000 K. For longer pulses, the maximum evaporation rate was calculated to be more or less constant for different pulse durations, because it depends merely on the laser irradiance, which is kept fixed. The evaporation rate decreases even slightly, because of increased plasma shielding for the longer pulses (see below), resulting in a somewhat lower net laser irradiance reaching the target. Because the evaporation rate is more or less constant, the total evaporation depth increases linearly with the pulse duration. Indeed, evaporation takes place as long as the laser pulse is on (and typically a bit longer); hence, a longer laser pulse can yield a larger amount of evaporation.

When the laser fluence is kept fixed at 10.6 J/cm^2, the maximum surface temperature and evaporation rate drop with increased pulse duration, as is clear from Fig. 12b. Note that the surface temperature calculated for the laser pulse of 1 ns is probably again too high, for the reasons indicated in Section 3.1.1. The drop in maximum surface temperature and in evaporation rate is logical because the laser irradiance drops, and the latter determines the maximum surface temperature, which in turn defines the

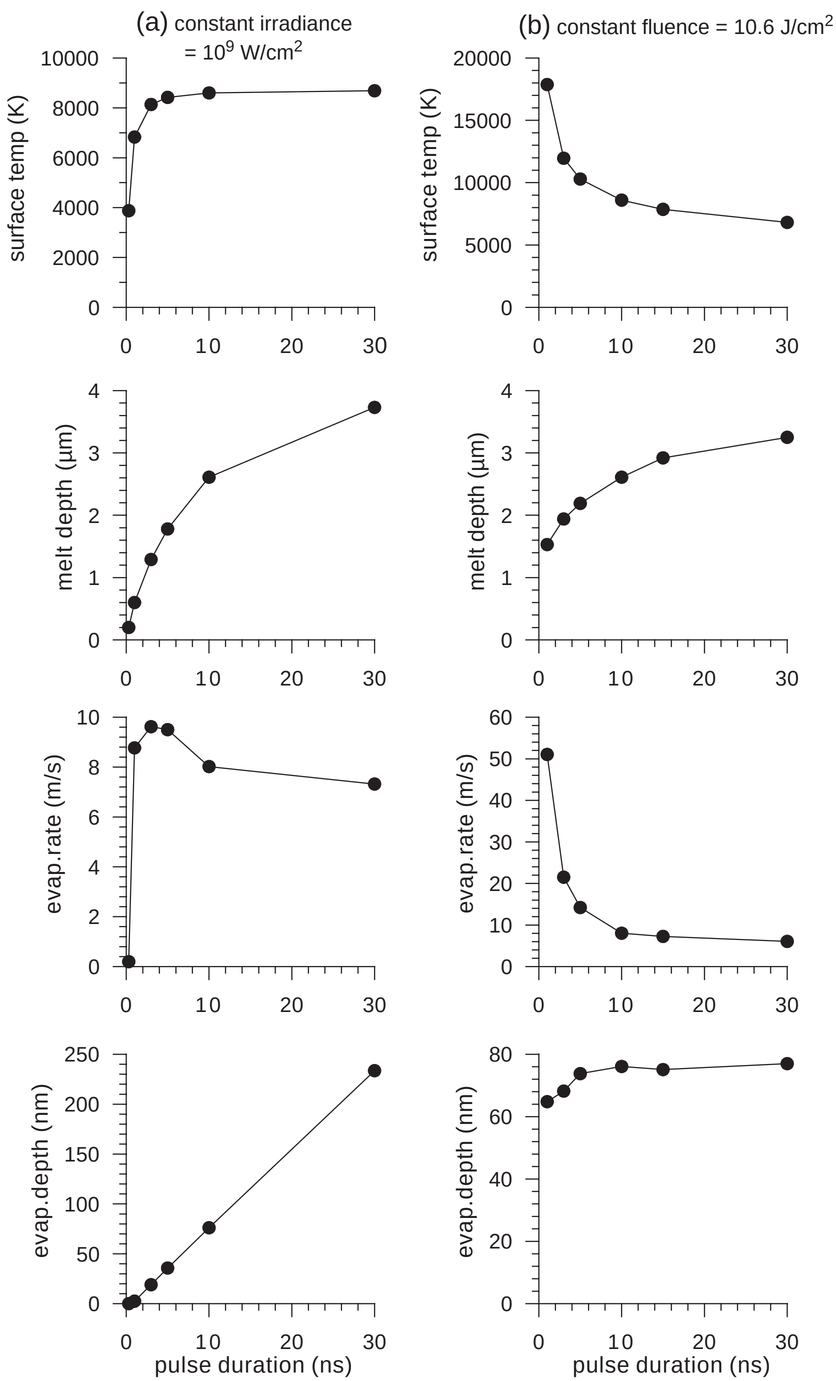

Fig. 12. Calculated maximum surface temperature, maximum melt depth, maximum evaporation rate, and total evaporation depth, as a function of pulse duration, for laser radiation of 266 nm, (a) at constant laser irradiance of 10^9 W/cm^2 (and therefore increasing laser fluence), and (b) at fixed laser fluence of 10.6 J/cm^2 (and hence decreasing values of laser irradiance).

maximum evaporation rate. Mao et al. investigated the effect of laser pulse length on the mass ablation rate, using an excimer laser of 248 nm and 30 ns pulse duration, and a Nd:YAG laser of 1064, 532 and 266 nm, with either 3 ns or 35 ps pulse duration, at a laser energy of 2 mJ for the Nd:YAG laser, and 5 mJ for the excimer laser, and they also observed a higher mass ablation rate for shorter laser pulses, when keeping the laser energy constant [40].

Further, as appears from Fig. 12b, our calculations predict an increase in the melt depth for longer pulses, because the target is exposed for a longer time to the laser, and moreover, as will be shown below, the plasma shielding becomes less severe for longer laser pulses (at constant laser fluence, and hence lower laser irradiance), so that the laser energy reaching the target will become somewhat larger. In spite of the drop in maximum evaporation rate, the total evaporation depth rises slightly with increasing pulse duration, which is also attributed to the somewhat higher energy reaching the target, as a result of reduced plasma shielding.

3.2.2. Evaporated plume expansion and plasma formation

The detailed spatial profiles of vapor density, background gas density, plume velocity and temperature, ionization fractions and densities of ions and electrons are not shown here for the different laser pulse durations, because they look qualitatively the same as the profiles in Figs. 3–5. Instead, the calculation results at 100 ns are plotted as a function of pulse duration, in Figs. 13 and 14, keeping either the laser irradiance fixed at 10^9 W/cm^2 so that the total laser fluence is different (Fig. 13), or at constant laser fluence of 10.6 J/cm^2 while the laser irradiance is changed (Fig. 14).

At constant laser irradiance, a longer pulse means a higher fluence reaching the target, resulting in more evaporation (see Fig. 12a, above), and hence in a higher vapor density. This is reflected in both the maximum vapor density (Fig. 13a) and in the vapor plume length (Fig. 13d). Moreover, the plume velocity (Fig. 13c) and temperature (Fig. 13 f) also become higher with increasing pulse duration. The larger amount of vapor pushes the He background gas further away from the target (Fig. 13e) and results also in a larger pile-up of background gas (Fig. 13b). Note the slight decrease in plume length and shock front position for a pulse duration of 30 ns. This is attributed to the fact that the evaporation process starts somewhat later in time, i.e., the maximum laser irradiance is only reached at about 40 ns, whereas for a pulse of 10 ns, the maximum irradiance is reached at about 12 ns (see Fig. 15). Hence, at 100 ns the evaporated Cu atoms have traveled for a shorter time, in the case of a 30 ns pulse, resulting in a somewhat shorter plume length, and consequently shock front position, despite of the larger total amount of evaporation.

As a result of the higher plume temperature (Fig. 13f), the amount of ionization increases with pulse duration, at constant laser irradiance, leading to a higher electron density (Fig. 13i) and a higher degree of ionization of Cu and He (Fig. 13g and h, respectively). Indeed, the fractions of Cu^0 and He^0 atoms drop, and the fractions of ions rise, for longer laser pulses. Note that the fraction of Cu^+ ions first increases, and then decreases again, when the Cu^{2+} ions become more important. All these trends are in fact very logical, because the total fluence increases with pulse duration, at constant laser irradiance.

When the laser fluence is kept constant, while increasing the laser pulse duration, the total amount of evapo-

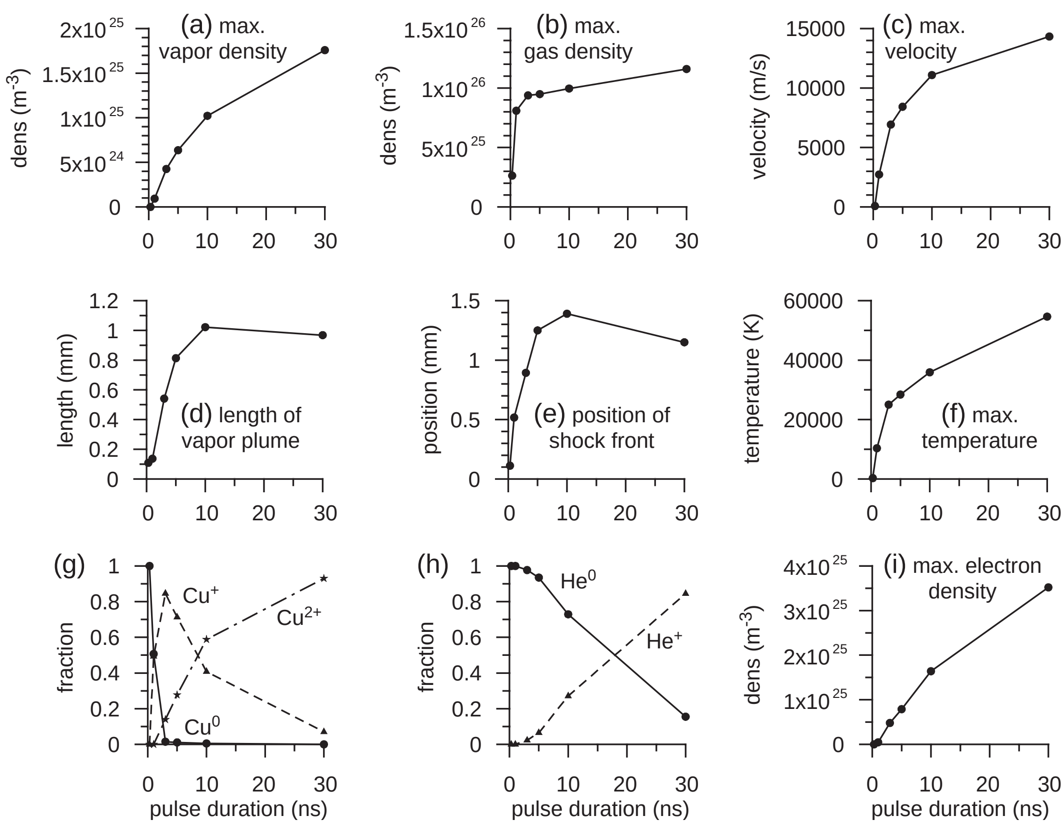

Fig. 13. Calculated maximum vapor number density (a), maximum background gas number density (b), maximum plume velocity (c), length of the vapor plume (d), shock front position (e), maximum temperature (f), fraction of Cu^0 atoms, Cu^+ and Cu^{2+} ions (g), fraction of He^0 atoms and He^+ ions (h), and maximum electron number density in the plume (i), all at 100 ns, for laser radiation of 266 nm, as a function of pulse duration, at constant laser irradiance of 10^9 W/cm^2 (and therefore increasing values of laser fluence).

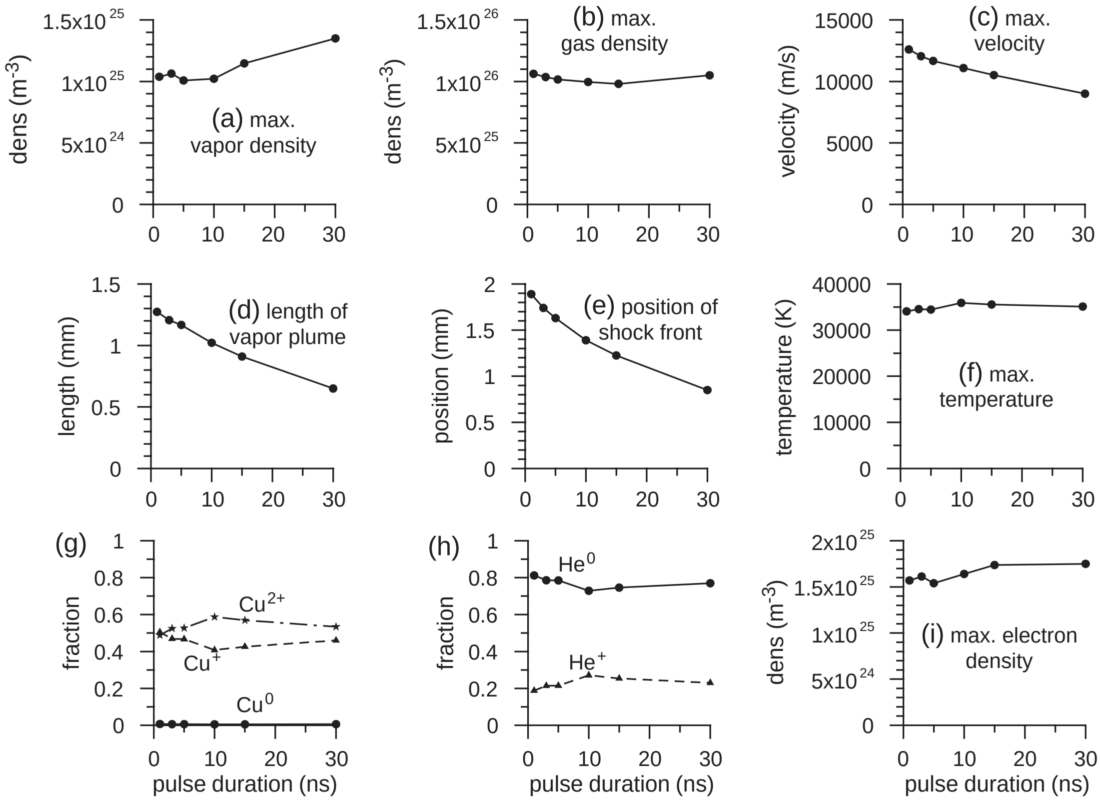

Fig. 14. Calculated maximum vapor number density (a), maximum background gas number density (b), maximum plume velocity (c), length of the vapor plume (d), shock front position (e), maximum temperature (f), fraction of Cu^0 atoms, Cu^+ and Cu^{2+} ions (g), fraction of He^0 atoms and He^+ ions (h), and maximum electron number density in the plume (i), all at 100 ns, for laser radiation of 266 nm, as a function of pulse duration, at constant laser fluence of 10.6 J/cm^2 (and therefore decreasing values of laser irradiance).

ration was found to be more or less constant (see Fig. 12b, above). As appears from Fig. 14, our calculations predict a slight increase in the maximum vapor density (Fig. 14a), and a drop in the plume length at 100 ns (Fig. 14d), so that the total amount of vapor in the plume will be more or less constant, in accordance with the total amount of evaporation. The maximum plume velocity (Fig. 14c) decreases slightly with plume length, due to the lower laser irradiance, resulting in a lower surface temperature (cf. Fig. 12b, above), and this indeed explains the shorter plume length at 100 ns. The maximum background gas density (Fig. 12b) appears to be independent from the laser pulse duration, but it is not pushed so far away from the target, as is clear from Fig. 12e, which is again attributed to the lower plume velocity. Note that the shorter plume length and shock front position at longer laser pulses are also partly due to the fact that the laser evaporation starts later in time, because the maximum laser irradiance is reached at a later time, compared to shorter pulses (cf. Fig. 15). Further, it is observed that the maximum plume temperature at 100 ns is more or less independent from the pulse duration (cf. Fig. 12f), and this applies also to the ionization fractions of Cu and He (Fig. 12g and h) and the electron density (Fig. 12i). Hence, it can be concluded from Fig. 14 that, except for a drop in the plume length and shock front position, the laser pulse duration has no significant effect on the plume behavior at a fixed moment in time (for instance, in our case at 100 ns), as long as the total fluence is kept constant. Similar conclusions were also drawn from experiments [36,38], albeit for different pulse durations (i.e., a comparison between a 10 ns and a 50 ps laser pulse in [36], and between laser pulses of 270 ps, 5 ps and 500 fs in [38]). Therefore, it seems that the total fluence is a more determining factor for the plume

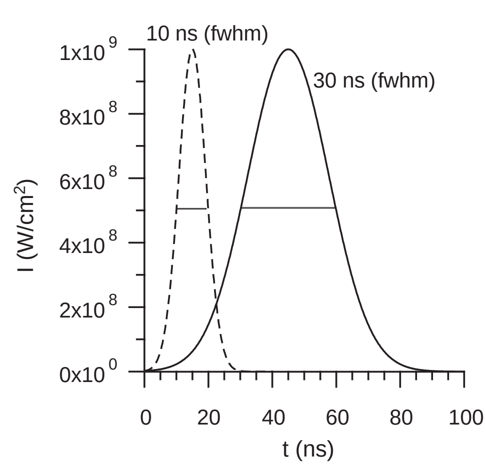

Fig. 15. Laser irradiance–time profile for a pulse of 10 ns fwhm (dashed line) and 30 ns fwhm (solid line).

behavior, at a fixed moment in time, than the pulse duration, and hence maximum laser irradiance.

This is also illustrated in Fig. 16, which depicts the maximum plume temperature (a) and maximum electron density (b), as well as the shock front position (c) as a function of time, for the different laser pulses, when keeping the total fluence constant. It is indeed observed that the maximum plume temperature and electron density are nearly independent from the pulse duration, for observation times of 40 ns and more (except for the electron density in the case of the 30 ns pulse, which reaches similar values as the other electron densities only after 80 ns). However, during the laser pulse, some differences become apparent. For a laser pulse of 1 ns, which corresponds to a laser irradiance of 10^{10} W/cm^2 at the fixed fluence of 10.6 J/cm^2, the maximum plume temperature was calculated to be higher than 100,000 K, leading to a maximum electron density of nearly 4×10^{27} m^{-3} at 2 ns (i.e., during the laser pulse). For a laser pulse of 3 ns, corresponding to a laser irradiance of 3.33×10^9 W/cm^2, the maximum plume temperature and electron density were about 80,000 K and almost 2×10^{27} m^{-3}, respectively, at 3–4 ns. This trend is continued: the maximum plume temperature and electron density during the laser pulse go down for longer pulses, because of the lower laser irradiance at fixed fluence. However, after a sufficiently long time (for instance, 40 ns at the conditions under study), when the influence of the laser pulse is not so clearly felt anymore (except for the 30 ns pulse), the maximum plume temperature and electron density become independent of the pulse duration, and only the total laser fluence counts, as discussed above. The shock front position, on the other hand, appears to be affected by the laser pulse duration, also for longer times, as appears from Fig. 16c, and as was also clear from Fig. 14e. Indeed, it decreases slightly with increasing pulse duration, because of the somewhat lower plume velocity, as well as the short delay in the evaporation process, as was explained above.

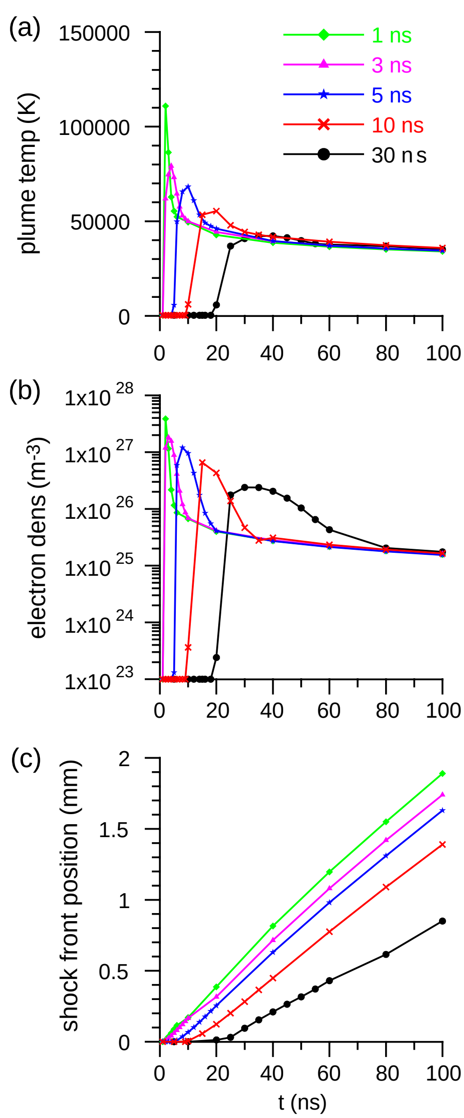

Fig. 16. Calculated maximum values of plume temperature (a) and electron number density (b), and calculated shock front position (c), as a function of time up to 100 ns, for laser radiation of 266 nm and constant fluence of 10.6 J/cm^2, at five different laser pulse durations (and therefore five different values of laser irradiance).

3.2.3. Laser absorption in the plasma

The calculated relative amount of laser absorption in the plasma, as well as the relative contributions of the three different absorption mechanisms, are presented in Fig. 17. As was already anticipated above, when discussing Fig. 12a and b, the percentage absorption, i.e., plasma shielding, increases with pulse duration, when the laser irradiance was kept constant (Fig. 17a), because of the larger fluence and hence higher densities of Cu vapor, electrons and ions (see Fig. 13). For a pulse of 0.3 ns, no plasma shielding is found to occur, whereas for a pulse duration of 30 ns, the plasma absorption amounts to almost 70%.

When the laser fluence is fixed, Fig. 17b illustrates that the relative amount of plasma absorption decreases with increasing pulse duration, due to the lower laser irradiance. For a pulse duration of 1 ns, corresponding to a laser irradiance of 10^{10} W/cm^2, the fraction of absorption is calculated to be 66%, whereas for a pulse of 30 ns, with laser irradiance of 3.33×10^8 W/cm^2, the plasma shielding is found to be about 40%. Because of this drop in plasma shielding for longer laser pulses, at constant laser fluence, the total melt depth and evaporation depth increase, in spite of the lower laser irradiance (see Fig. 12b). It could also be deduced from our model calculations that for shorter laser pulses, plasma shielding only occurs at higher laser irradiance, or in other words, that the laser irradiance threshold for plasma shielding increases for shorter laser pulses. This is also confirmed from experiments [26]. Indeed, it is found that a Nd:YAG laser with 35 ps pulse duration yields a roll-off in the ICP-AES emission intensity, which indicates the threshold for plasma shielding (see

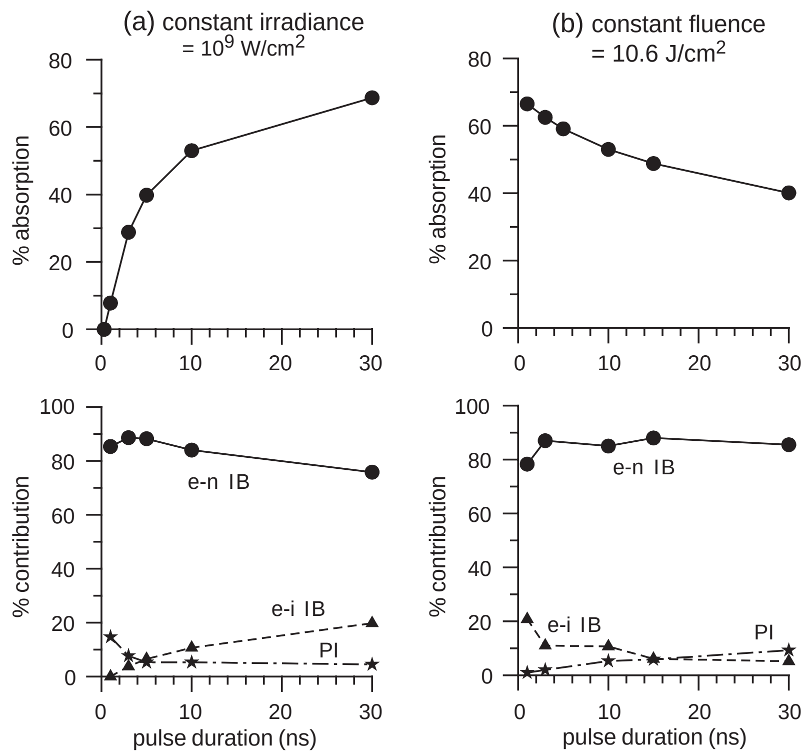

Fig. 17. Calculated relative amount of laser absorption in the plasma, and calculated relative contributions of electron–neutral and electron–ion inverse Bremstrahlung (e–n IB and e–i IB) and photo-ionization (PI) as absorption mechanisms, for laser radiation of 266 nm, as a function of laser pulse duration, (a) at constant laser irradiance of 10^9 W/cm^2 (and therefore increasing laser fluence), and (b) at fixed laser fluence of 10.6 J/cm^2 (and hence decreasing values of laser irradiance).

above), at a laser irradiance of 2×10^{10} W/cm^2, whereas the same roll-off was observed at about 3×10^8 W/cm^2 for an excimer laser with 30 ns pulse duration [26].

Finally, as far as the relative contributions of different laser absorption mechanisms are concerned, it is observed in Fig. 17 that e–n IB always constitutes the main absorption mechanism, whereas e–i IB and PI contribute for 20% or less, for all laser pulses investigated.

3.3. Effect of laser wavelength

Up to now, we have focused in our calculation results on a laser wavelength of 266 nm, which is the fourth harmonic of a Q-switched Nd:YAG laser. We have, however, also applied our model to other laser wavelengths, used by either Nd:YAG lasers or excimer lasers. The effect of laser wavelength, as treated in our model, is twofold: it determines both the laser absorption in the plasma, as well as in the target.

First, as is clear from the two formulas presented above (in Section 3.1), the laser absorption in the plasma, by e–n IB and e–i IB, depends on the laser wavelength. The common factor in both formulas $(1-\exp(-hc/\lambda kT))$, which accounts for stimulated emission [74], will drop with increasing wavelength. On the other hand, the e–i IB absorption coefficient also increases with λ^3. Hence, the general outcome of the effect of laser wavelength on the overall absorption in the plasma will depend on the relative contribution of these two opposing effects, as will be demonstrated below. Furthermore, the laser absorption by PI also depends on the laser wavelength, or photon energy, as discussed above in Section 3.1. Indeed, a longer wavelength corresponds to a lower photon energy, and hence, a lower probability for PI from the excited levels, resulting in a lower PI absorption coefficient.

Second, the effect of the laser wavelength on the target behavior is reflected in a different target surface reflectivity for different wavelengths. Indeed, it was reported in [30,42] that the reflectivity of Cu is 0.97, 0.61 and 0.34 for 1064 nm, 532 nm and 266 nm, respectively. Hence, at 1064 nm, only 3% of the laser energy can penetrate into the target, resulting in heating, melting and vaporization, and the remaining energy is simply reflected from the surface, whereas at 266 nm, 66% of the laser energy can be used for target heating, melting and vaporization.

Based on these considerations, we have applied our model also to a Nd:YAG laser at the fundamental wavelength (1064 nm) and at its second harmonic (532 nm), in order to compare with the calculation results at 266 nm. It is worth to mention that we have also performed calculations for different UV wavelengths, typically used in Nd:YAG and excimer lasers, but the effect of laser wavelength was then not so pronounced, due to the relatively smaller differences in wavelength values. Hence, we will focus here only on the comparison between Nd:YAG lasers of 1064, 532 and 266 nm.

3.3.1. Target heating, melting and vaporization

Fig. 18 shows the calculated maximum surface temperature (a), maximum melt depth (b), maximum evaporation rate (c) and evaporation depth (d) as a function of laser irradiance, for the three wavelengths investigated. Again, the surface temperature in the order of 15,000 K, as calculated for the higher laser irradiance values, is probably overestimated, for the reasons mentioned in Section 3.1.1. The difference between 266 and 532 nm is found to be relatively small. Indeed, at 532 nm, the target reflectivity is higher than at 266 nm (0.61 vs. 0.34; see above), yielding a lower amount of laser energy available for penetration in the sample, but on the other hand, our model predicts less plasma shielding at 532 nm, as will be discussed below. These competing effects almost compensate each other, so that the surface temperature, melt depth, evaporation rate and depth calculated for the laser of 532 nm are only slightly lower than at 266 nm. The difference with the wavelength of 1064 nm, on the other hand, is much more pronounced. Indeed, the target reflectivity is assumed to be 0.97, so that only 3% of the laser radiation can penetrate into the sample. For instance, at a laser irradiance of 10^9 W/cm^2, target melting and evaporation do not yet take place. Target melting only occurs for a laser irradiance above 2×10^9 W/cm^2, and target evaporation comes only into play at a laser irradiance of 6×10^9 W/cm^2, as appears from Fig. 18. Similarly, for the same laser irradiance, the surface temperature, melt depth, evaporation rate and depth are calculated to be much lower at 1064 nm than at 266 and 532 nm. The fact that shorter wavelengths yield more efficient laser ablation was also found experimentally [28,39–41], although it should be mentioned that in Ref. [42] the opposite tendency was observed. Horn et al. [29] did not see a clear difference in the ablation rate, but they compared a wavelength of 266 and 193 nm, in which case the difference was also found to be negligible in our calculations.

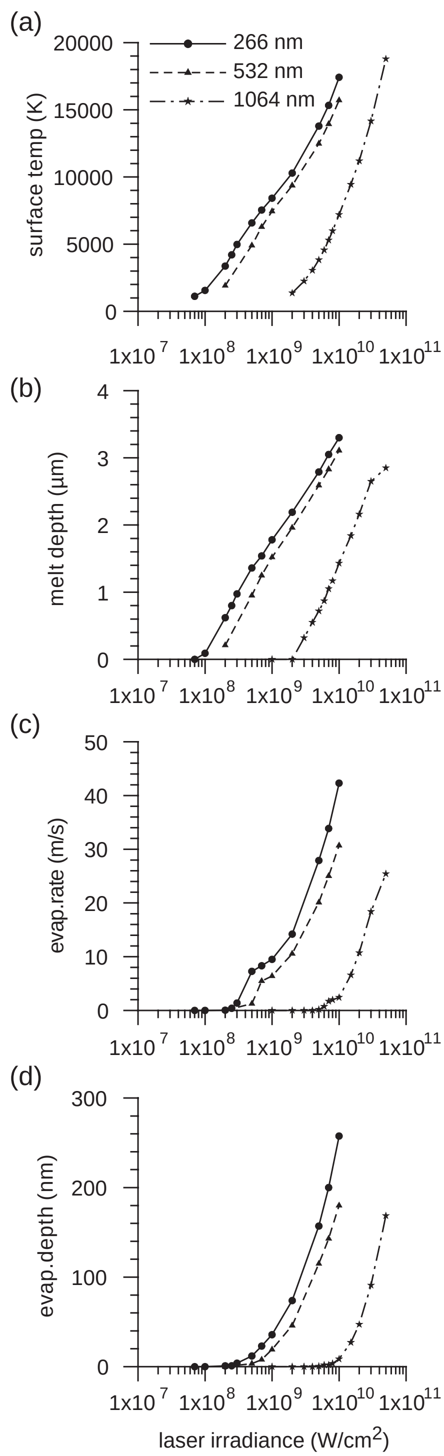

Fig. 18. Calculated maximum surface temperature (a), maximum melt depth (b), maximum evaporation rate (c) and evaporation depth (d), as a function of laser irradiance, for three different laser wavelengths.

3.3.2. Evaporated plume expansion and plasma formation

Due to the relatively small difference in target evaporation behavior between 266 and 532 nm, as predicted by our model, the plume characteristics (i.e., vapor density, velocity, temperature, ionization degree, etc) at 532 nm were also found to be only slightly lower than at 266 nm, and the results at 532 nm are therefore not shown here, because they resemble the calculation results at 266 nm (see before, e.g., Figs. 3–6), with only a slight reduction in calculation values.

At 1064 nm, on the other hand, the difference is much more pronounced. Fig. 19 illustrates the effect of laser irradiance on the plume characteristics, for the laser irradiance of 1064 nm. Note that the laser irradiance is now varied between 10^9 and 10^{11} W/cm^2, hence it is shifted with one order of magnitude compared to the case of 266 nm (cf. Fig. 6 above). Indeed, at 1064 nm, the target evaporation started only to become important at a laser irradiance above 5×10^9 W/cm^2.

As is apparent from Fig. 19, once target evaporation comes into play, the plume characteristics (i.e., plume

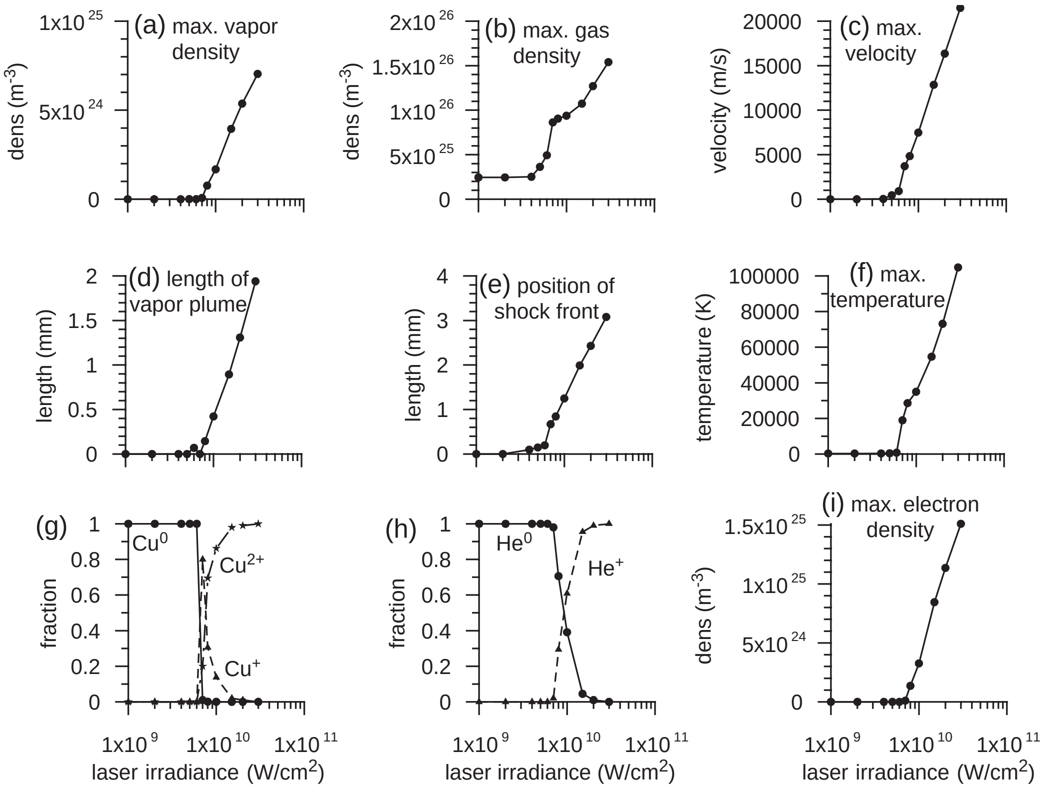

Fig. 19. Calculated maximum vapor number density (a), maximum background gas number density (b), maximum plume velocity (c), length of the vapor plume (d), shock front position (e), maximum temperature (f), fraction of Cu^0 atoms, Cu^+ and Cu^{2+} ions (g), fraction of He^0 atoms and He^+ ions (h), and maximum electron number density in the plume (i), all at 100 ns, as a function of laser irradiance, for laser radiation of 1064 nm and 5 ns pulse duration.

length, densities, velocity, temperature, ionization degree) all increase drastically with laser irradiance, and the rise is much more pronounced than at 266 nm. For instance, at a laser irradiance below or equal to 6×10^9 W/cm^2, no plasma is formed yet, and only Cu and He atoms are present in the plume. At 7×10^9 W/cm^2, a plasma is created, and suddenly the Cu^+ ions become the dominant Cu species, but at 8×10^9 W/cm^2, the Cu^{2+} ions reach already the highest density of all Cu species. In other words, plasma formation occurs only at a higher laser irradiance, but once a plasma is formed, the temperature, ionization degree and electron density increase rapidly to high values. The fact that a higher laser irradiance was needed to produce a plasma at 1064 nm was also observed in Ref. [46].

3.3.3. Laser absorption in the plasma

Fig. 20 depicts the calculated percentage laser absorption in the plasma, as a function of laser irradiance, for the three laser wavelengths (Fig. 20a), as well as the relative contributions of e–n IB, e–i IB and PI, computed for 266 and 532 nm (Fig. 20b). It is clear from Fig. 20a that the plasma absorption is predicted to be lower at higher laser wavelengths. This is in contradiction with the suggestions made in the literature (e.g., [39,42]), that higher laser wavelengths yield more plasma absorption, because of the λ^3-dependence of the e–i IB coefficient (see Eq. (2) above). However, as was indicated above, both e–n IB and e–i IB coefficients also contain a common factor $(1-\exp(-hc/\lambda kT))$, which accounts for stimulated emission [74], and this factor drops with increasing wavelengths. At typical plume temperatures of 20,000–50,000 K, as found in our calculations, the above factor is more or less inversely proportional with the wavelength, i.e., increasing the wavelength by a factor of 4 (from 266 to 1064 nm) yields a drop in this factor by a factor of 4. The λ^3-dependency is of course stronger, but it only affects the e–i IB absorption coefficient.

At 266 nm, e–n IB is found to be the dominant absorption mechanism at all laser irradiance values investigated, although its relative contribution drops as a function of laser irradiance, accompanied by a rise in e–i IB (see grey lines in Fig. 20b). At 532 nm, the e–n IB absorption coefficient drops by roughly a factor 2 compared with 266 nm (see discussion above), whereas the e–i IB coefficient increases (due to the λ^3-dependency, although this is partly compensated by the stimulated emission factor; see above). However, the net effect is still a somewhat lower amount of plasma absorption at 532 nm, because of the big impact of e–n IB at 266 nm, and also due to the slightly lower electron, ion and neutral densities in the plasma at 532 nm. The effect is larger at the lower laser irradiance values, where e–n IB is also the dominant absorption mechanism at 532 nm, and it is less pronounced at the higher laser irradiance values, where e–i IB is

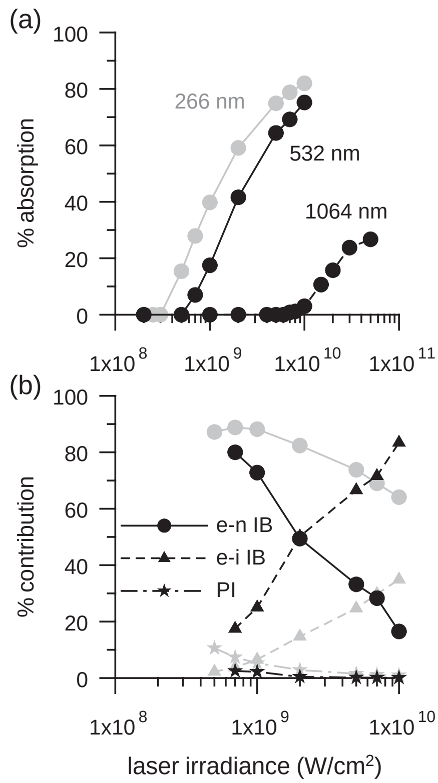

Fig. 20. Calculated relative amount of laser absorption in the plasma (a), and calculated relative contributions of electron–neutral and electron–ion inverse Bremstrahlung (e–n IB and e–i IB) and photo-ionization (PI) as absorption mechanisms (b), as a function of laser irradiance, for three different laser wavelengths and 5 ns pulse duration. The data in figure (b) represent only the results at 266 nm (grey curves) and 532 nm (black curves), because at 1064 nm, it is predicted that e–i IB accounts for 100% of the plasma absorption (therefore not shown).

dominant at 532 nm (see black lines in Fig. 20b). For instance, at 10^9 W/cm^2, where e–n IB is dominant at both laser wavelengths, the % absorption is calculated to be 40% at 266 nm and 17.5% at 532 nm, whereas at 10^{10} W/cm^2, where e–i IB is more important at 532 nm, the % absorption is calculated to be 82% and 75%, for 266 and 532 nm, respectively.

At 1064 nm, the amount of plasma absorption is much lower than at 266 and 532 nm, in spite of the fact that the e–i IB absorption coefficient is significantly higher. This is due to the much lower densities of electrons, ions and neutrals in the plasma (see above), because of the much lower amount of evaporation. Because the e–i IB absorption coefficient increases with laser wavelength, and the e–n IB and PI coefficients drop with wavelength, our model predicts that at 1064 nm, the plasma absorption is entirely due to e–i IB (therefore not shown explicitly in Fig. 20b).

Based on the lower amount of plasma absorption at 532 nm, as predicted by our model, it can now also be understood why the surface temperature, melt depth, evaporation rate and depth were calculated to be quite similar at 532 and 266 nm (cf. Fig. 18 above). Indeed, the laser energy effectively penetrating the sample can be approximated as:

$$E \sim I_0(1-R)(1-A)$$

where I_0, R and A stand for the original laser irradiance, the target reflectivity and the % absorption in the plasma, respectively. Inserting the corresponding values for 266 and 532 nm at a laser irradiance of 10^9 W/cm^2, yields:

- at 266 nm: $E \sim 10^9\ (1-0.34)\ (1-0.4) = 3.96 \times 10^8$
- at 532 nm: $E \sim 10^9\ (1-0.61)\ (1-0.175) = 3.22 \times 10^8$

This corresponds to a relative difference of only 20%. The relative difference in surface temperature is still somewhat lower, but this is because there is no linear relationship between the laser energy penetrating into the sample, and the maximum surface temperature. Indeed, the deposited energy is divided in several parts, i.e., thermal convective loss (heating), melting and vaporization enthalpy, and kinetic energy of the evaporated material.

Finally, it should be realized that these results are a bit unexpected, in view of the suggestions made in literature, about increasing plasma absorption at higher wavelengths. However, by carefully analyzing and checking quantitatively our calculation results, the obtained outcome seems logical to us. Of course, everything depends on the accuracy of the assumed target surface reflectivities, and e–n IB and e–i IB absorption coefficients, which were adopted from literature, and which are probably subject to uncertainties. Nevertheless, the overall results of our model, such as melt and evaporation depths, vapor velocity, plume length and temperature, etc. appear to be quite realistic, based on comparison with experiments. Therefore, the present quantitative analysis might shed a new light on the effect of laser wavelength, if the plasma absorption and target reflectivity coefficients are reliable.

4. Conclusion

A comprehensive numerical model for ns-LA of metallic targets, based on target heating, melting and vaporization, plume expansion in 1 atm background gas, plasma formation and laser absorption in the plasma, was recently developed [12], and is applied here to investigate the effect of laser parameters, such as laser irradiance, pulse duration and wavelength, on the target and plume characteristics, for a wide range of conditions, typical for LA and LIBS. Table 2 gives an overview of the calculation results obtained with the model.

It is found that target heating, melting and vaporization, as well as the vapor and background gas density, plume expansion velocity and temperature, ionization degree and densities of ions and electrons in the plume, and hence also the plasma shielding all increase with laser irradiance. The model predicts that the threshold for target melting is around

Table 2
Overview of the typical calculation results that have been obtained with the model

Target:
• Temperature distribution inside the target
• Melt depth
• Evaporation depth
• Evaporation rate
Plume/plasma:
• Vapor density as a function of position in the plume
• Background gas density as a function of position in the plume
• Plume velocity as a function of position in the plume
• Plume temperature as a function of position in the plume
• Ionization degree; fraction of Cu^0, Cu^+, Cu^{2+}, He^0, He^+ as a function of position in the plume
• Densities of Cu^0, Cu^+, Cu^{2+}, He^0, He^+ and electrons as a function of position in the plume
• Position of plume shock front
Laser absorption in the plasma:
• % absorption of the laser
• % contribution of electron–neutral inverse Bremsstrahlung (e–n IB), electron–ion inverse Bremsstrahlung (e–i IB), and photo-ionization (PI) to the total absorption
• Absorption coefficients of these processes, as a function of position in the plume

10^8 W/cm^2, at a laser wavelength of 266 nm and a pulse duration of 5 ns. The threshold for target vaporization is found to be about $2-3\times10^8$ W/cm^2, and the laser irradiance threshold for plasma formation is predicted to be between 3 and 5×10^8 W/cm^2.

The effect of laser pulse duration shows two different trends, depending on whether the laser irradiance or laser fluence is kept constant. At constant laser irradiance, the target heating, melting and vaporization increase with laser pulse duration, and this applies also to the densities of vapor and background gas atoms and ions, and electrons in the plume, as well as to the plume expansion velocity and temperature, because the laser fluence rises with pulse duration. At fixed laser fluence, on the other hand, the target heating and evaporation rate increase for shorter laser pulses, because of the rise in laser irradiance. The total melt and evaporation depth increase slightly for longer laser pulses, because the target is exposed to the laser for a longer time, and it is found that the plasma shielding is a bit less pronounced for longer pulses, because of the lower irradiance, so that the net laser fluence reaching the target increases slightly with pulse duration. The plume temperature and electron density, during or shortly after the laser pulse, become higher for shorter pulses, because of higher laser irradiance at fixed laser fluence. However, at a certain moment in time, sufficiently long after the laser pulse is finished (e.g., 100 ns), it is observed that the total laser fluence, and not the pulse duration, determines the plume behavior, because the plume and plasma characteristics look very similar for different pulse durations, at constant laser fluence.

Finally, the effect of laser wavelength was investigated. The calculated target and plume characteristics (e.g., surface temperature, melt and evaporation depth, plume density, velocity, temperature, ionization degree in the plasma,. . .) at 532 nm were only slightly lower than at 266 nm, because of the competing effects of target surface reflectivity and laser plasma absorption. At 1064 nm, the target and plume characteristics were calculated to be significantly lower than at 266 and 532 nm, mainly attributed to the high surface reflectivity of 0.97, leaving only 3% of the laser energy available for target heating, melting and vaporization. It was found that the laser irradiance threshold for target melting and vaporization and for plasma formation at 1064 nm was considerably higher than at 266 and 532 nm, or in other words, that the shorter wavelengths yielded more efficient laser ablation than the 1064 nm wavelength, in correspondence with literature findings.

Our calculation results have been compared with experimental data as much as possible, and in general reasonable agreement is obtained, so that it can be concluded that our model presents a more or less realistic picture of laser ablation of metals, plume expansion in 1 atm He and plasma formation, for a wide range of conditions of laser irradiance, pulse duration (in the ns-range) and laser wavelength.

In the near future, we wish to apply the model to a variety of target materials, in order to compare their behavior, and we also plan to investigate the effect of different background gases on the laser ablation and plume behavior [72]. Future plans also include the extension of the model to two dimensions, to include expansion in the radial direction, and the incorporation of nano-particle formation by condensation and the formation of larger particulates by liquid splashing, in order to obtain a better understanding of the particle formation mechanisms in LA.

Acknowledgments

This research is financed by a Bilateral Project between Flanders and China. The authors thank A. Vertes for supplying the original code for laser ablation in vacuum, and A. Vertes and R. Gijbels for the interesting discussions.

References

[1] M.C. Galicia, A. Vertes, J.H. Callahan, Atmospheric pressure matrix-assisted laser desorption/ionization in transmission geometry, Anal. Chem. 74 (2002) 1891–1895.
[2] A. Vertes, R. Gijbels, F. Adams (Eds.), Laser Ionization Mass Analysis, Wiley, New York, 1993.
[3] L.J. Radziemski, From LASER to LIBS, the path of technology development, Spectrochim. Acta, Part B: Atom. Spectrosc. 57 (2002) 1109–1113.
[4] J.D. Winefordner, I.B. Gornushkin, T. Correll, E. Gibb, B.W. Smith, N. Omenetto, Comparing several atomic spectrometric methods to the super stars: special emphasis on laser induced breakdown spectrometry, LIBS, a future super star, J. Anal. At. Spectrom. 19 (2004) 1061–1083.
[5] J.M. Vadillo, J.J. Laserna, Laser-induced plasma spectrometry: truly a surface analytical tool, Spectrochim. Acta, Part B: Atom. Spectrosc. 59 (2004) 147–161.

[6] R.E. Russo, Laser ablation, Appl. Spectrosc. 49 (1995) 14A–28A.
[7] D. Günther, S.E. Jackson, H.P. Longerich, Laser ablation and arc/spark solid sample introduction into inductively coupled plasma mass spectrometers, Spectrochim. Acta, Part B: Atom. Spectrosc. 54 (1999) 381–409.
[8] B. Hattendorf, C. Latkoczy, D. Günther, Laser ablation inductively coupled plasma mass spectrometry—it's the aerosol size that really matters in this high-throughput technique for ultratrace analysis of solids, Anal. Chem. 75 (2003) 341A–347A.
[9] L. Balazs, R. Gijbels, A. Vertes, Expansion of laser-generated plumes near the plasma ignition threshold, Anal. Chem. 63 (1991) 314–320.
[10] A. Bogaerts, Z. Chen, R. Gijbels, A. Vertes, Laser ablation for analytical sampling: what can we learn from modeling?, Spectrochim. Acta, Part B: Atom. Spectrosc. 58 (2003) 1867–1893.
[11] A. Bogaerts, Z. Chen, Nanosecond laser ablation of Cu: modeling of the expansion in He background gas, and comparison with expansion in vacuum, J. Anal. At. Spectrom. 19 (2004) 1169–1176.
[12] Z. Chen, A. Bogaerts, Laser ablation of Cu and plume expansion into 1 atm ambient gas, J. Appl. Physi. 97 (2005) 063305, (12 pages).
[13] M. Aden, E. Beyer, G. Herziger, H. Kunze, Laser-induced vaporization of a metal surface, J. Phys., D, Appl. Phys. 25 (1992) 57–65.
[14] J.R. Ho, C.P. Grigoropoulos, J.A.C. Humphrey, Computational study of heat transfer and gas dynamics in the pulsed laser evaporation of metals, J. Appl. Physi. 78 (1995) 4696–4709.
[15] A. Vertes, Energy coupling and dissipation mechanisms in laser–solid interaction, in: J.C. Miller, D.B. Geohegan (Eds.), Laser Ablation: Mechanisms and Applications-II, AIP Conference Proceedings, vol. 288, AIP Press, New York, 1994.
[16] M. Capitelli, F. Capitelli, A. Eletskii, Non-equilibrium and equilibrium problems in laser-induced plasmas, Spectrochim. Acta, Part B: Atom. Spectrosc. 55 (2000) 559–574.
[17] G. Callies, H. Schittenhelm, P. Berger, H. Hügel, Modeling of the expansion of laser-evaporated matter in argon, helium and nitrogen and the condensation of clusters, Appl. Surf. Sci. 127–129 (1998) 134–141.
[18] A.V. Gusarov, A.G. Gnedovets, I. Smurov, Gas dynamics of laser ablation: influence of ambient atmosphere, J. Appl. Physi. 88 (2000) 4352–4364.
[19] A.G. Gnedovets, A.V. Gusarov, I. Smurov, A model for nanoparticle synthesis by pulsed laser evaporation, J. Phys., D, Appl. Phys. 32 (1999) 2162–2168.
[20] A.V. Gusarov, A.G. Gnedovets, I. Smurov, G. Flamant, Simulation of nanoscale particles elaboration in laser-produced erosive flow, Appl. Surf. Sci. 154–155 (2000) 331–336.
[21] A.V. Gusarov, I. Smurov, Near-surface laser–vapour coupling in nanosecond pulsed laser ablation, J. Phys., D, Appl. Phys. 36 (2003) 2962–2971.
[22] S.S. Mao, X. Zeng, X. Mao, R.E. Russo, Laser-induced breakdown spectroscopy: flat surface vs. cavity structures, J. Anal. At. Spectrom. 19 (2004) 495–498.
[23] H.C. Liu, X.L. Mao, J.H. Yoo, R.E. Russo, Early phase laser induced plasma diagnostics and mass removal during single-pulse laser ablation of silicon, Spectrochim. Acta, Part B: Atom. Spectrosc. 54 (1999) 1607–1624.
[24] H.C. Liu, X.L. Mao, J.H. Yoo, R.E. Russo, Nonlinear changes in plasma and crater properties during laser ablation of Si, Appl. Phys. Lett. 75 (1999) 1216–1218.
[25] L.A. Doyle, G.W. Martin, A. Al-Khateeb, I. Weaver, D. Riley, M.J. Lamb, T. Morrow, C.L.S. Lewis, Electron number density measurements in magnesium laser produced plumes, Appl. Surf. Sci. 127–129 (1998) 716–720.
[26] M.A. Shannon, X.L. Mao, A. Fernandez, W.T. Chan, R.E. Russo, Laser ablation mass removal vs. incident power density during solid sampling for inductively coupled plasma-atomic emission spectroscopy, Anal. Chem. 67 (1995) 4522–4529.
[27] J.H. Yoo, O.V. Borisov, X. Mao, R.E. Russo, Existence of phase explosion during laser ablation and its effects on inductively coupled plasma-mass spectrometry, Anal. Chem. 73 (2001) 2288–2293.
[28] R. Fabbro, E. Fabre, F. Amiranoff, G. Garban-Labaune, J. Virmont, M. Weinfeld, C.E. Max, Laser wavelength dependence of mass-ablation rate and heat-flux inhibition in laser-produced plasmas, Phys. Rev., A 26 (1982) 2289–2292.
[29] I. Horn, M. Guillong, D. Günther, Wavelength dependant ablation rates for metals and silicate glasses using homogenized laser beam profiles—implications for LA–ICP-MS, Appl. Surf. Sci. 182 (2001) 91–102.
[30] S. Conesa, S. Palanco, J.J. Laserna, Acoustic and optical emission during laser-induced plasma formation, Spectrochim. Acta, Part B: Atom. Spectrosc. 59 (2004) 1395–1401.
[31] W.T. Chan, R.E. Russo, Study of laser–material interaction using inductively coupled plasma-atomic emission spectrometry, Spectrochim. Acta, Part B: Atom. Spectrosc. 46 (1991) 1471–1486.
[32] S.H. Jeong, O.V. Borisov, J.H. Yoo, X.L. Mao, R.E. Russo, Effects of particle size distribution on inductively coupled plasma mass spectrometry signal intensity during laser ablation of glass samples, Anal. Chem. 71 (1999) 5123–5130.
[33] O.V. Borisov, X. Mao, R.E. Russo, Effects of crater development on fractionation and signal intensity during laser ablation inductively coupled plasma mass spectrometry, Spectrochim. Acta, Part B: Atom. Spectrosc. 55 (2000) 1693–1704.
[34] G.P. Pinho, H. Schittenhelm, W.W. Duley, S.A. Schlueter, H.R. Jahani, R.E. Mueller, Energy distributions in the laser ablation of metals and polymers, Appl. Surf. Sci. 127–129 (1998) 983–987.
[35] W. Sdorra, K. Niemax, Basic investigations for laser microanalysis: III. Application of different buffer gases for laser-produced sample plumes, Mikrochim. Acta 107 (1992) 319–327.
[36] G.W. Rieger, M. Taschuk, Y.Y. Tsui, R. Fedosejevs, Comparative study of laser-induced plasma emission from microjoule picosecond and nanosecond KrF-laser pulses, Spectrochim. Acta, Part B: Atom. Spectrosc. 58 (2003) 497–510.
[37] H. Borchert, K. Darée, M. Hugenschmidt, Plasma formation during the interaction of picosecond and nanosecond laser pulses with BK7 glass, J. Phys., D, Appl. Phys. 38 (2005) 300–305.
[38] B. Le Drogoff, J. Margot, F. Vidal, S. Laville, M. Chaker, M. Sabsabi, T.W. Johnston, O. Barthélemy, Influence of the laser pulse duration on laser-produced plasma properties, Plasma Sources Sci. Technol. 13 (2004) 223–230.
[39] X.L. Mao, O.V. Borisov, R.E. Russo, Enhancements in laser ablation inductively coupled plasma-atomic emission spectrometry based on laser properties and ambient environment, Spectrochim. Acta, Part B: Atom. Spectrosc. 53 (1998) 731–739.
[40] X.L. Mao, A.C. Ciocan, O.V. Borisov, R.E. Russo, Laser ablation processes investigated using ICP-AES, Appl. Surf. Sci. 127–129 (1998) 262–268.
[41] R.E. Russo, X.L. Mao, O.V. Borisov, H. Liu, Influence of wavelength on fractionation in laser ablation ICP-MS, J. Anal. At. Spectrom. 15 (2000) 1115–1120.
[42] L.M. Cabalin, J.J. Laserna, Experimental determination of laser induced breakdown thresholds of metals under nanosecond Q-switched laser operation, Spectrochim. Acta, Part B: Atom. Spectrosc. 53 (1998) 723–730.
[43] M. Guillong, D. Günther, Effect of particle size distribution on ICP-induced elemental fractionation in laser ablation–inductively coupled plasma-mass spectrometry, J. Anal. At. Spectrom. 17 (2002) 831–837.
[44] M. Guillong, I. Horn, D. Günther, A comparison of 266 nm, 213 nm and 193 nm produced from a single solid state Nd:YAG laser for laser ablation ICP-MS, J. Anal. At. Spectrom. 18 (2003) 1224–1230.
[45] J. Gonzales, X.L. Mao, J. Roy, S.S. Mao, R.E. Russo, Comparison of 193, 213 and 266 nm laser ablation ICP-MS, J. Anal. At. Spectrom. 17 (2002) 1108–1113.
[46] G. Abdellatif, H. Imam, A study of the laser plasma parameters at different laser wavelengths, Spectrochim. Acta, Part B: Atom. Spectrosc. 57 (2002) 1155–1165.

[47] V. Detalle, M. Sabsabi, L. St. Onge, A. Hamel, R. Héon, Influence of Er:YAG and Nd:YAG wavelengths on laser-induced breakdown spectroscopy measurements under air or helium atmosphere, Appl. Opt. 42 (2003) 5971–5977.

[48] S.H. Jeong, R. Greif, R.E. Russo, Propagation of the shock wave generated from excimer laser heating of aluminum targets in comparison with ideal blast wave theory, Appl. Surf. Sci. 127–129 (1998) 1029–1034.

[49] A. Gomes, A. Aubreton, J.J. Gonzalez, S. Vacquié, Experimental and theoretical study of the expansion of a metallic vapour plasma produced by laser, J. Phys., D, Appl. Phys. 37 (2004) 689–696.

[50] J.H. Yoo, S.H. Jeong, R. Greif, R.E. Russo, Explosive change in crater properties during high power nanosecond laser ablation of silicon, J. Appl. Phys. 88 (2000) 1638–1649.

[51] Q. Lu, S.S. Mao, X. Mao, R.E. Russo, Delayed phase explosion during high-power nanosecond laser ablation of silicon, Appl. Phys. Lett. 80 (2002) 3072–3074.

[52] Q. Lu, Thermodynamic evolution of phase explosion during high-power nanosecond laser ablation, Phys. Rev., E Stat. Phys. Plasmas Fluids Relat. Interdiscip. Topics 67 (2003) 016410.

[53] J.G. Lunney, R. Jordan, Pulsed laser ablation of metals, Appl. Surf. Sci. 127–129 (1998) 941–946.

[54] S. Amoruso, Modelling of laser produced plasma and time-of-flight experiments in UV laser ablation of aluminium targets, Appl. Surf. Sci. 138–139 (1999) 292–298.

[55] A. Kar, J. Mazumder, Mathematical model for laser ablation to generate nanoscale and submicrometer-size particles, Phys. Rev., B 49 (1994) 410–419.

[56] B. Sallé, C. Chaléard, V. Detalle, J.L. Lacour, P. Mauchien, C. Nouvellon, A. Semerok, Laser ablation efficiency of metal samples with UV laser nanosecond pulses, Appl. Surf. Sci. 138–139 (1999) 302–305.

[57] V. Hohreiter, J.E. Carranza, D.W. Hahn, Temporal analysis of laser induced plasma properties as related to laser-induced breakdown spectroscopy, Spectrochim. Acta, Part B: Atom. Spectrosc. 59 (2004) 327–333.

[58] V.S. Burakov, N.V. Tarasenko, N.A. Savastenko, Plasma chemistry in laser ablation processes, Spectrochim. Acta, Part B: Atom. Spectrosc. 56 (2001) 961–971.

[59] G. Callies, P. Berger, H. Hügel, Time-resolved observation of gas-dynamic discontinuities arising during excimer laser ablation and their interpretation, J. Phys., D, Appl. Phys. 28 (1995) 794–806.

[60] R. Noll, R. Sattmann, V. Sturm, S. Winkelmann, Space- and time-resolved dynamics of plasmas generated by laser double pulses interacting with metallic samples, J. Anal. At. Spectrom. 19 (2004) 419–428.

[61] A. Peterlongo, A. Miotello, R. Kelly, Laser-pulse sputtering of aluminum: vaporization, boiling, superheating, and gas-dynamic effects, Phys. Rev., E Stat. Phys. Plasmas Fluids Relat. Interdiscip. Topics 50 (1994) 4716–4727.

[62] Z. Zhang, Z.-X. Han, G.S. Dulikravich, Numerical simulation of laser induced plasma during pulsed laser deposition, J. Appl. Phys. 90 (2001) 5889–5897.

[63] S.S. Harilal, C.V. Bindhu, M.S. Tillack, F. Najmabadi, A.C. Gaeris, Internal structure and expansion dynamics of laser ablation plumes into ambient gases, J. Appl. Phys. 93 (2003) 2380–2388.

[64] M.A. Hafez, M.A. Khedr, F.F. Elaksher, Y.E. Gamal, Characteristics of Cu plasma produced by a laser interaction with a solid target, Plasma Sources Sci. Technol. 12 (2003) 185–198.

[65] M. Capitelli, A. Casavola, G. Colonna, A. De Giacomo, Laser-induced plasma expansion: theoretical and experimental aspects, Spectrochim. Acta, Part B: Atom. Spectrosc. 59 (2004) 271–289.

[66] J. Hermann, C. Vivien, A.P. Carricato, C. Boulmer-Leborgne, A spectroscopic study of laser ablation plasmas from Ti, Al and C targets, Appl. Surf. Sci. 127–129 (1998) 645–649.

[67] E.M. Monge, C. Aragón, J.A. Aguilera, Space- and time-resolved measurements of temperatures and electron densities of plasmas formed during laser ablation of metallic samples, Appl. Phys., A Mater. Sci. Process. 69 (1999) S691–S694.

[68] J.A. Aguilera, J. Bengoechea, C. Aragón, Spatial characterization of laser induced plasmas obtained in air and argon with different laser focusing distances, Spectrochim. Acta, Part B: Atom. Spectrosc. 59 (2004) 461–469.

[69] M. Corsi, G. Cristoforetti, M. Giuffrida, M. Hidalgo, S. Legnaioli, V. Pelleschi, A. Salvetti, E. Tognoni, C. Vallebona, Three-dimensional analysis of laser induced plasmas in single and double pulse configuration, Spectrochim. Acta, Part B: Atom. Spectrosc. 59 (2004) 723–735.

[70] J.A. Aguilera, C. Aragón, Characterization of a laser induced plasma by spatially resolved spectroscopy of neutral atom and ion emissions. Comparison of local and spatially integrated measurements, Spectrochim. Acta, Part B: Atom. Spectrosc. 59 (2004) 1861–1876.

[71] G. Cristoforetti, S. Legnaioli, V. Palleschi, A. Salvetti, E. Tognoni, Influence of ambient gas pressure on laser induced breakdown spectroscopy technique in the parallel double-pulse configuration, Spectrochim. Acta, Part B: Atom. Spectrosc. 59 (2004) 1907–1917.

[72] A. Bogaerts, Z.Y. Chen, UV laser ablation of various metals in different background gases: comparative study by numerical modeling, in preparation.

[73] J.F. Ready, Effects of High Power Laser Radiation, Academic Press, New York, 1971.

[74] L.J. Rakziemski, D.A. Cremers (Eds.), Laser-Induced Plasmas and Applications, Marcel Dekker Inc., New York, 1989.

[75] P.J. Shayler, M.T.C. Fang, The transport and thermodynamic properties of a copper–nitrogen mixture, J. Phys., D, Appl. Phys. 10 (1977) 1659–1669.

[76] S. Amoruso, R. Bruzzese, N. Spinelli, R. Velotta, Characterization of laser-ablation plasmas, J. Phys., At. Mol. Opt. Phys. 32 (1999) R131–R172.

[77] S.S. Mao, X. Mao, R. Greif, R.E. Russo, Initiation of an early-stage plasma during picosecond laser ablation of solids, Appl. Phys. Lett. 77 (2000) 2464–2466.

[78] X.L. Mao, W.T. Chan, M.A. Shannon, R.E. Russo, Plasma shielding during picosecond laser sampling of solid materials by ablation in He vs. Ar atmosphere, J. Appl. Phys. 74 (1993) 4915–4922.

[79] S.S. Mao, X. Mao, R. Greif, R.E. Russo, Simulation of a picosecond laser ablation plasma, Appl. Phys. Lett. 76 (2000) 3370–3372.

[80] S.S. Mao, X.-L. Mao, R. Greif, R.E. Russo, Simulation of infrared picosecond laser-induced electron emission from semiconductors, Appl. Surf. Sci. 127–129 (1998) 206–211.

[81] J. Güdde, J. Hohlfeld, J.G. Müller, E. Matthias, Damage threshold dependence on electron–phonon coupling in Au and Ni films, Appl. Surf. Sci. 127–129 (1998) 40–45.

[82] H.E. Elsayed-Ali, T.B. Norris, M.A. Pessot, G.A. Mourou, Time-resolved observation of electron–phonon relaxation in copper, Phys. Rev. Lett. 58 (1987) 1212–1215.

[83] S.S. Wellershoff, J. Hohlfeld, J. Güdde, E. Matthias, The role of electron–phonon coupling in femtosecond laser damage of metals, Appl. Phys., A Mater. Sci. Process. 69 (1999) S99–S107.